

國立臺灣大學理學院物理學系

碩士論文

Department of Physics

College of Science

National Taiwan University

Master Thesis



以光鑷與協同冷卻實現可擴展的離子阱量子電腦
Scalable Quantum Computing with an Ion Crystal
Stabilized by Tweezers and Sympathetic Cooling

沈于晴

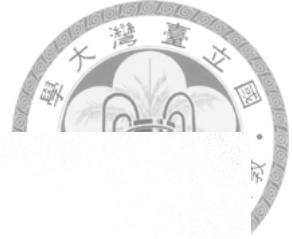
Yu-Ching Shen

指導教授：林俊達博士

Advisor: Guin-Dar Lin, Ph.D.

中華民國 106 年 12 月

December, 2017



國立臺灣大學碩士學位論文
口試委員會審定書

Scalable Quantum Computing with an Ion Crystal
Stabilized by Tweezers and Sympathetic Cooling

本論文係沈于晴君 (R03222059) 在國立臺灣大學物理學系完成之碩士學位論文，於民國 106 年 12 月 29 日承下列考試委員審查通過及口試及格，特此證明

口試委員：

林俊達

張銘顯

管希聖

所長：



誌謝

經過漫長的時間，終於完成畢業論文了。首先要感謝我的指導教授林俊達老師。在老師自由且不失嚴謹的指導下，我對量子光學、量子計算與如何做研究有了更深的感覺。感謝張銘顯老師與管希聖老師的建議，使這份論文更加完善。感謝實驗室的各位夥伴：冠廷、婷姐、鎮宇、澤霈、爾祥、可維、資莘、智圓、享菴，除了平常的討論和閒聊外，在我需要幫忙時也一定可以得到你們的幫助。感謝「屁哥讀書會」的隊友們：博亞、善長、銘峰、力弘。在各自為研究奮鬥的同時，我很享受跟你們一起讀統物、讀量物、讀場論，當然還有天南地北瞎扯的時光。你們是我最大的精神支柱。感謝同在 502 裡打拼的安良學長、泰尹、丞翔、仁宇，以及時常來 502 串門子的老錢、重陽、蕎東、小高、沂璇。此外，感謝國術社與校隊的彥竹、翊蕾、權元、兆平、岱蓉、珮恂、謝慈、稚然、韋君、大大大、不缺；以及一起吃拉麵的基隆人們：聖倫、爆哥、浩宸。你們讓我的研究生生活從不乏味。最後，最重要的，感謝我的爸媽無條件支持，讓我沒後顧之憂；感謝我可愛的妹妹無時無刻不幫我加油打氣。我愛你們！



摘要

如何擴展離子阱量子電腦一直以來是一項挑戰，其困難主要來自穩定離子陣列以及克服背景雜訊造成的加熱。在實現量子邏輯閘的操控上，由於要求雷射光能準確照射在某個特定的離子量子位元而不影響鄰近位元，離子間的距離必須大於雷射光寬度，而這個間距的數量級大約為微米等級。在常用的無線電頻率（radio-frequency, RF）離子阱架構下，當離子的數目越來越多時，軸向的束縛頻率須越來越小，以保持離子間距。故當大型離子陣列用於量子計算時，首要困難就是軸向模態的頻率趨近於零，使得該方向振動難以冷卻。因此我們提出在大型離子陣列中加入光鑷來固定離子，借此引入了新的軸向振動頻率。我們計算了當離子處於背景加熱時在協同冷卻下達到穩定態時的位置不準量。我們發現光鑷增加了軸向的穩定度。此外，光鑷阻擋了徑向模態的熱傳導。這個特性保護了在不同區域的量子邏輯閘不受彼此的影響，由此可以實行平行運算。等效來說，我們可以將兩個光鑷間的離子視為一段「局部離子阱」。我們計算了局部離子阱的冷卻效率以及探討其弛豫動力學。

關鍵字：離子阱、可擴展量子計算、光鑷、協同冷卻



Abstract

Scalability of quantum computing based on trapped ions in a linear radio-frequency trap has been a challenge due to instability of crystallization and heating. To construct a large-scale ion array with single qubit addressability, the ions' spacing must be kept a few times larger than or at least comparable to the beam size, which is of the order of microns. This implies that the longitudinal confinement vanishes as the number of ions gets very large. Meanwhile, the collective motional modes of very low frequencies are easily thermally populated and hard to be cooled. We thus propose a scalable scheme combining the applications of optical tweezers and sympathetic cooling. We demonstrate that for a large-scale ion chain, the application of optical tweezers raises the lowest longitudinal frequency by effectively pinning the ions in space. We calculate the steady-state profile of ions' position fluctuations given that the system exposes to heat and is also sympathetically cooled at the same time. We find that the optical tweezers can enhance the stability of the longitudinal arrangement. Also, it blocks heat propagation of the transverse motion, suggesting that the qubit gate operation based on transverse modes can be done in parallel and thus protected by optical tweezers. This allows us to deal with only a portion defined by two edge ions that are illuminated by tweezer beams. This segment of the ion array is confined by a "local trap" provided by two effectively pinned ions. We demonstrate the relevant cooling efficiency and discuss the relaxation dynamics.

Keywords: ion trap, scalable quantum computation, optical tweezers, sym-

pathetic cooling





Contents

口試委員會審定書	ii
誌謝	iii
摘要	iv
Abstract	v
1 Introduction	1
1.1 Motivation	1
1.2 Paul trap	3
1.3 Universal quantum gate	5
1.3.1 Cirac-Zoller gate	7
1.3.2 Mølmer-Sørensen gate	8
1.3.3 Geometrical phase gate	10
1.4 Transverse-mode scheme	12
1.5 Cooling in trapped ions	13
1.6 Thesis outline	14
2 Collective motion of trapped ions with optical tweezers	15
2.1 Overview	15
2.2 Normal modes of the harmonic trap	16
2.3 Normal modes when applying optical tweezers	17

3 Sympathetic cooling for large-scale computing	23
3.1 Overview	23
3.2 Model	24
3.3 Steady state	27
3.3.1 Thermal equilibrium	27
3.3.2 Sympathetic cooling	28
3.4 Steady state profile with optical tweezers	30
3.4.1 Longitudinal modes for periodic arrangement of tweezers	30
3.4.2 Transverse mode for periodic arrangement of tweezers	34
3.5 Local trap	37
3.6 Relaxation dynamics	40
3.7 Gate design	40
3.8 Chapter summary	41
4 Conclusion	44
A Gate design	47
Bibliography	51





List of Figures

1.1	The analogous figure of Paul trap. A particle is confined in a rotating saddle-shaped potential surface.	4
1.2	The schematic figure of an ion trap device. (a) The standard Paul trap formed by four parallel wires. (b) The surface-electrode ion trap [19]. . .	4
1.3	The energy level of a trapped ion. The green, blue, and red arrows correspond to the carrier, blue sideband and red sideband transitions respectively.	5
1.4	The concept of the Cirac-Zoller gate.	8
1.5	The concept of the Mølmer-Sørensen gate. Bichromatic laser beams are applied on the ions. The intermediate states are not populated because of the off resonance. The overall transitions are $ ggn\rangle \leftrightarrow een\rangle$ (left panel) and $ egn\rangle \leftrightarrow gen\rangle$. These paths interfere destructively and eliminate the dependence of phonon number n [10].	9
1.6	The concept of the geometrical phase gate. If the ions' internal state is $ eg\rangle$ or $ ge\rangle$, the motional state displaces in the phase space. At the end of the gate operation, the motional state goes back to the origin and gains a phase corresponding to the area of the closed loop.	12
2.1	Optical tweezers are applied on the ions (nodes), who are arranged periodically on the chain.	16
2.2	The equilibrium position of ions. The length unit is z_s . The dotted line shows the separation between central ions decreases as number of ions increases [31].	20



2.3 The normal mode frequencies of ions. The frequency unit is trapping frequency ω_z . $\omega_{x(y)} = 10\omega_z$ 20

2.4 The (a)(c)(e)(g) longitudinal and (b)(d)(f)(h) transverse mode frequencies of 13 ions applied by optical tweezers periodically with the tweezers period (a)(b) 12, (c)(d) 6, (e)(f)4, and (g)(h)3. 21

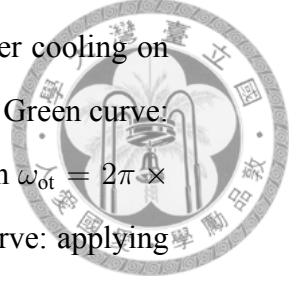
2.5 The mode frequency of the lowest mode. $^{171}\text{Yb}^+$ ions are trapped with the minimal spacing $d_0 = 10 \mu\text{m}$. We apply optical tweezers periodically on the first of every 10 ions. 22

3.1 The architecture of sympathetic cooling. The cooling ions play a role of the heat drain. The computational ions will be cooled through the heat exchange due to the Coulomb interaction. 25

3.2 (a)(b)The position fluctuation and (c)(d) its corresponding infidelity of 21 $^{171}\text{Yb}^+$ ions with minimum separation $d_0 = 10 \mu\text{m}$ under Doppler temperature $T_D = 0.5 \text{ mK}$. ($k_B T_D / \hbar = 2\pi \times 10 \text{ Mhz} = 70\omega_0$.) Other parameters: $\omega_z = 2\pi \times 34 \text{ kHz} = 0.24\omega_0$, $\omega_x = 5.1 \text{ MHz} = 35.7\omega_0$, $|\Delta\mathbf{k}|d_0 = 157$, and $w = 0.25d_0$ [17]. 28

3.3 The steady state profile of 21 ions under sympathetic cooling with different background temperature. 5 ions on the both ends are cooled continuously. The ideal case corresponds to the thermal equilibrium profile under T_D . $\omega_z = 0.24\omega_0$, $\omega_x = 36\omega_0$ [17]. 30

3.4 The steady profile of 121 ions under periodic sympathetic cooling. The index of the cooling ions are $i = 1, 11, \dots, 121$. For $i \in C$, $\gamma_i = 0.1\omega_0$, $T_i = T_D$. For $i \in H$, $\gamma_{\text{bg}} = 10^{-10}\omega_0$, $T_{\text{bg}} = 10^6 T_D$. $\omega_z = 2\pi \times 7.2 \text{ kHz} = 0.05\omega_0$, $\omega_x = 2\pi \times 5.1 \text{ MHz} = 36\omega_0$ [17]. 31



3.5 The position fluctuation of longitudinal mode under sympathetic cooling associated with optical tweezers. Blue curve: applying laser cooling on one of 10 ions. Red dotted curve: all the ions are under T_D . Green curve: applying laser cooling associated with optical tweezers with $\omega_{ot} = 2\pi \times 200 \text{ kHz} = 1.4\omega_0$ on one of every 10 ions. Magenta dotted curve: applying optical tweezers on one of every 10 ions while all of ions are under T_D . Other parameters are same as Figure 3.4. 32

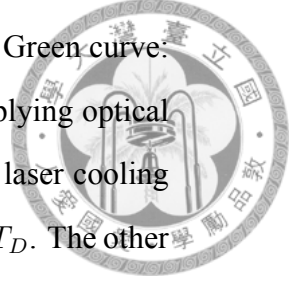
3.6 The average of position fluctuation δz_{avg} versus the ion number N . We make the minimum separation of ions $d_0 = 10 \mu\text{m}$ for every N 33

3.7 The position fluctuation of transverse mode under sympathetic cooling associated with optical tweezers. We can see that the ions have large position fluctuation when we turn the optical tweezers. Blue curve: applying laser cooling on one of 10 ions. Red dotted curve: all the ions are under T_D . Green curve: applying laser cooling associated with optical tweezers with on one of every 10 ions. The parameters are same as Figure 3.5. . . . 34

3.8 The position fluctuation of transverse mode under sympathetic cooling. The optical tweezers are applied on the heating ions. Cooling ions: $i = 1, 11, \dots, 121$. Pinned ions: $i = 23, 49, 69, 87$. The other parameters are same as Figure 3.5 36

3.9 The position fluctuation of the transverse mode. (a)Cooling ions: $i = 1, 11, \dots, 121$. Pinned ions: $i = 42, 50, 92, 100$. (b)Cooling ions: $i = 42, 50, 92, 100$. Pinned ions: $i = 41, 51, 91, 101$. The other parameters are same as Figure 3.5 36

3.10 The setup of the local trap. 37



- 3.11 The position fluctuations of (a) longitudinal and (b) transverse mode. Blue curve: applying laser cooling on the 31st and the 41st ions. Green curve: applying laser cooling on the 31st and the 41st ions and applying optical tweezers on 30th and 42nd ions. Magenta curve: applying laser cooling on one of every 10 ions. Red dotted line: every ion is under T_D . The other parameters are same as Figure 3.5. 38
- 3.12 The position fluctuation profile of the local trap for $N = 121$. (a)(b)(c): Longitudinal mode. (d)(e)(f): Transverse mode. (a)(d): cooling ions: $i = 11, 21$, pinned ions: $i = 10, 22$. (b)(e): cooling ions: $i = 31, 41$, pinned ions: $i = 30, 42$. (c)(f): cooling ions: $i = 51, 61$, pinned ions: $i = 50, 62$. Blue curve: Turn off the optical tweezers. Green curve: Turn on the optical tweezers. Red curve: every ion is under T_D without the tweezers. The parameters are same as Figure 3.5. 39
- 3.13 The time evolution of δz_i (a)(b)(c) and δx_i (d)(e)(f) for different segments of local traps. The cooling and pinned ions of each subfigure are same as Figure 3.12 The ion chain is under $T = 10T_D$ at $t = 0$. The other parameters are same as Figure 3.5. 41
- 3.14 Quantum gate design for $N = 121$. Cooling ions: 51, 61. Pinned ions: 50, 62. Gate ions: 55, 57. (a)The fidelity with different gate time and laser frequency. (b) The laser shape with $\tau = 500\tau_0$ and $\mu = 0.982\omega_x$ (denoted by the arrow in (a)). $\delta F = 10^{-13}$. The other parameters are same as Figure 3.5. 43



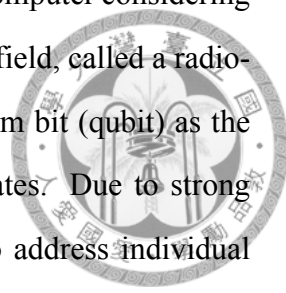
Chapter 1

Introduction

1.1 Motivation

Quantum computation can efficiently solve some problems which are considered difficult to be solved by means of a classical one. For instance, the integer factorization problem, the discrete logarithm problem, and the ellipse curve discrete logarithm problem can be speed up exponentially by Shor's algorithm [1, 2]. Taking the integer factorization problem for example, the largest integer that has been factorized up to now is 232 decimal digit long (~ 768 digits in binary) [3]. It takes about 2 years with hundreds of parallel machines to factorize such a number. It can be estimated that, with Shor's algorithm, the computation time can be reduced to shorter than a week [4]. For practical uses, in 2000 D. P. Divincenzo proposed a checklist of requirements that a promising quantum computer fulfills, known as Divincenzo's criteria [5]:

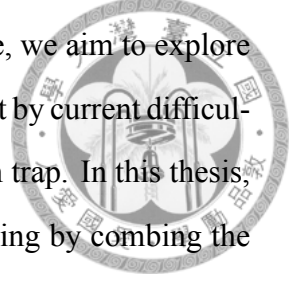
1. It is a scalable physical system with well characterized qubits.
2. It has the ability to initialize the state of the qubits to a simple fiducial state.
3. The qubit has long relevant coherence time, which is much longer than the gate operating time.
4. It has a universal set of quantum gate.
5. It has a qubit-specific measurement capability.



Ion traps are regarded as one of the leading candidates of a quantum computer considering these conditions. Ions are confined in space by time-varying electric field, called a radio-frequency (RF) trap, or a Paul trap [6]. Each ion serves as a quantum bit (qubit) as the quantum information is encoded in two of the atomic hyperfine states. Due to strong Coulomb repulsion, the ions are well separated thus allowing us to address individual ones. The initial state can be prepared by the optical pumping technique. The coherence time of the metastable state is about 0.1 seconds [7], while the gate operation time is about a few hundred microseconds. To implement a quantum logic gate, we shine laser beams on ions to manipulate transitions of internal states. There are several schemes for elementary logic gates, which can further constitute more complicated operations and functions. In addition to the original prototype, known as Cirac-Zoller gate, proposed by J. I. Cirac and P. Zoller in 1995 [8], the most commonly used scheme nowadays is the Mølmer-Sørensen gate, proposed by K. Mølmer and A. Sørensen [9, 10] in 1999. Both schemes will be briefly summarized in the succeeding discussions. The Mølmer-Sørensen gate can reach very high gate fidelity even when the ions are in thermal motion. To read out, one of the qubit states can be pumped to a short-lived auxiliary state, which will soon emit fluorescence, while the other state is left unchanged. Thus, the quantum state can be measured by detecting the photon statistics of the fluorescence [7]. The ion trap system has many advantages. For example, due to the strong and long range Coulomb interaction, the quantum gate can be made arbitrarily fast and involving distant ions. Further, since the quantum circuit is determined by the external laser, we can reconfigure the quantum circuit without altering the structure of the ion array. These features make an ion-trap based quantum computer even suitable for fabrication and easily re-programmable [11]. There are some quantum algorithms that have been already demonstrated in ion trap systems [11, 12].

However, like other physical platforms of implementation, scalability is the most serious challenge. The difficulty of stabilizing the ion array structure and cooling grows up as the number of ions increases. The main proposals of scaling up an ion trap include ion shuttling [13] and quantum networks [14]. These proposals raise other questions such as

precise control and adiabatic movement of ions, quantum interfacing between ion traps and other platforms that may involve flying qubits like photons. Here, we aim to explore and break the limitation with a simple linear Paul-trap configuration set by current difficulties, mostly associated with serious heating issues in a large-scale ion trap. In this thesis, we propose an all-ion based scheme for large-scale quantum computing by combing the ideas of local optical tweezers [15] and sympathetic cooling [16, 17].



1.2 Paul trap

We use a Paul trap to confine the ions [6]. The Paul trap is named after its inventor W. Paul, who won the Nobel Prize in Physics in 1989 for this contribution. From Earnshaw's theorem, we know that a charged particle cannot be captured stably in a static electric field. To circumvent the difficulty, a Paul trap uses a fast-oscillating quadrupole setting of electrodes, usually in radio-frequency, to offer an effective local trapping potential. The concept of a Paul trap is illustrated in Figure 1.1: Intuitively, under the quadrupole saddle-shaped potential surface shown in the left panel, a particle near the saddle point is supposed to move toward the potential minimum along the x axis but fall off along the y axis for the potential is a local maximum. But before the particle gets to leave the trap, the potential surface rotates about the z axis such that the potential along the y axis becomes a local minimum, as shown in the right panel, and pushes the particle back to the saddle point. As a consequence, the charged particle can be effectively confined as long as the rotating frequency of the quadrupole surface is appropriately chosen.

Figure 1.2 shows the schematic figure of a linear Paul trap, which is typically formed by 4 parallel wires. In Figure 1.2(a), two diagonal electrode wires are applied RF voltages, which yield an instantaneous potential $\Phi_{\text{RF}} = \frac{V_0 \cos \Omega t}{2} (1 + \frac{x^2 - y^2}{R^2})$ (R is a geometrical factor). Its time-averaged value is $U_{\text{eff}} = \frac{1}{2} m \omega_r^2 (x^2 + y^2)$, where $\omega_r = \frac{eV_0}{\sqrt{2} m \Omega R^2}$, m is the mass and e is the charge of a single ion [18]. The other two wires are segmented into different DC voltages along the z direction such that a local DC potential $\Phi_{\text{DC}} = \frac{\kappa U_0}{2z_0^2} (z^2 - \frac{1}{2}(x^2 + y^2))$ (κ, z_0 are geometrical factors) can be built to provide confinement along the wires. Combining the DC and RF parts, the effective potential energy in 3-

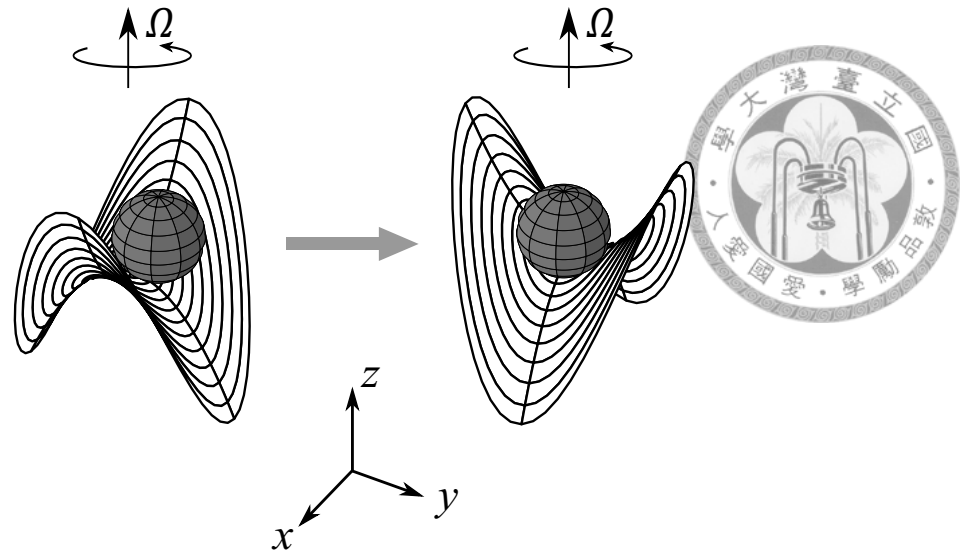


Figure 1.1: The analogous figure of Paul trap. A particle is confined in a rotating saddle-shaped potential surface.

dimension can be approximated by

$$U = \frac{1}{2}m\omega_x^2x^2 + \frac{1}{2}m\omega_y^2y^2 + \frac{1}{2}m\omega_z^2z^2,$$

where $\omega_z = \sqrt{\frac{e\kappa U_0}{mz_0^2}}$, and $\omega_x = \omega_y = \sqrt{\omega_r^2 - \frac{1}{2}\omega_z^2}$. Typically, $\omega_{x,y}$ is much larger than ω_z to make the ions aligned along the z axis. For recent development of the ion trap, some groups have started to construct ion traps on surfaces (Figure 1.2(b)) [19] for its advantages on easy fabrication, good accessibility, and simple electronic circuit design.

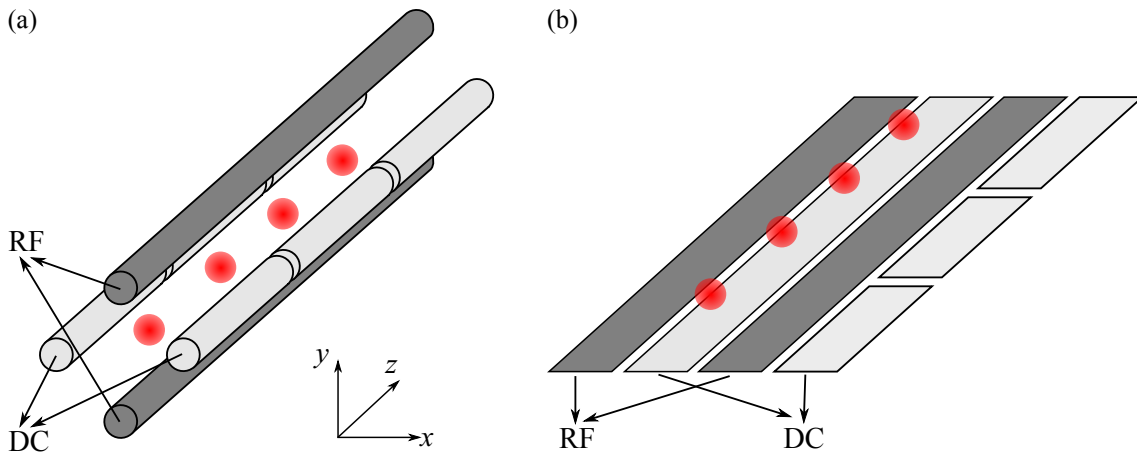


Figure 1.2: The schematic figure of an ion trap device. (a) The standard Paul trap formed by four parallel wires. (b) The surface-electrode ion trap [19].

1.3 Universal quantum gate

Any quantum circuit can be decomposed into single-qubit rotation gates and two-qubit entangling gates, e.g. control-NOT (CNOT) gates or control-phase-flip (CPF) gates [20]. This is called the universality of the quantum gates. In this section, we will discuss how to implement the universal gates with the trapped ions.

Suppose the information is encoded in an ion's hyperfine state $|g\rangle$ (ground state) and $|e\rangle$ (excited state). The energy separation between the two levels is $\hbar\omega_{eg}$. Consider a vibrational mode in a harmonic trap with an angular frequency ν , which can be described by the Fock basis $|n\rangle$. The energy configuration of the joint states of an ion is shown in Figure 1.3.

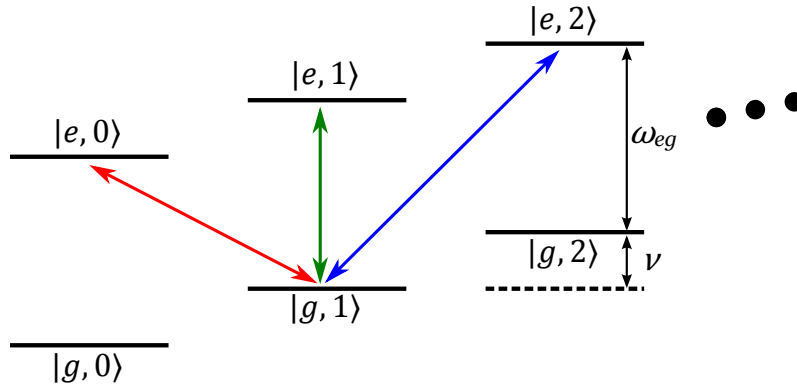


Figure 1.3: The energy level of a trapped ion. The green, blue, and red arrows correspond to the carrier, blue sideband and red sideband transitions respectively.

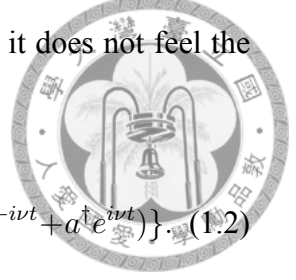
We now apply laser beams to drive transitions between these states. The Hamiltonian of the laser-ion interaction in the interaction picture reads [21]

$$H_I = \hbar\Omega\sigma^+ e^{-i(\delta t - \phi)} \exp(i\eta(ae^{-i\nu t} + a^\dagger e^{i\nu t})) + \text{H.c.}, \quad (1.1)$$

where Ω is the Rabi frequency of the laser, $\delta = \omega - \omega_{eg}$ is the laser-ion detuning, ϕ is the phase offset of the laser. $\sigma^+ = |e\rangle\langle g|$ and $\sigma^- = |g\rangle\langle e|$ are raising and lowering operators of the atomic states; a and a^\dagger are annihilation and creation operators of the phonon states; $\eta = k\sqrt{\frac{\hbar}{2m\nu}}$ is the Lamb-Dicke parameter with k the wavevector of the laser. The Lamb-Dicke parameter characterizes the ratio between the oscillation amplitude of the ion to

the wavelength of the laser. Taking the Lamb-Dicke limit $\eta\sqrt{n} \ll 1$, which means the displacement of the ion is much smaller than the wavelength so that it does not feel the spatial dependence of the field, the Hamiltonian becomes

$$H_I = \hbar\Omega\{\sigma^+ e^{-i(\delta t - \phi)} + \sigma^- e^{i(\delta t - \phi)} + i\eta(\sigma^+ e^{-i(\delta t - \phi)} - \sigma^- e^{i(\delta t - \phi)})(ae^{-i\nu t} + a^\dagger e^{i\nu t})\}. \quad (1.2)$$



Now we discuss the three cases of interest: $\delta = 0$, and $\delta = \pm\nu$ in the following, where we ignore the fast oscillating terms:

1. For $\delta = 0$ (carrier transition, shown by the green arrow in Figure 1.3), the laser couples $|g, n\rangle$ and $|e, n\rangle$. The Hamiltonian is

$$H = \hbar\Omega(\sigma^+ e^{i\phi} + \sigma^- e^{-i\phi}). \quad (1.3)$$

2. For $\delta = \nu$ (blue sideband transition, shown by the blue arrow in Figure 1.3), the laser couples $|g, n\rangle$ and $|e, n + 1\rangle$. The Hamiltonian is

$$H = i\hbar\Omega\eta(\sigma^+ a^\dagger e^{i\phi} - \sigma^- a e^{-i\phi}), \quad (1.4)$$

and we get the effective Rabi frequency

$$\Omega_{n,n+1} = \sqrt{n+1}\eta\Omega. \quad (1.5)$$

3. For $\delta = -\nu$ (red sideband transition, shown by the red arrow in Figure 1.3), the laser couples $|g, n\rangle$ and $|e, n - 1\rangle$. The Hamiltonian is

$$H = -i\hbar\Omega\eta(\sigma^+ a e^{i\phi} - \sigma^- a^\dagger e^{-i\phi}), \quad (1.6)$$

and the effective Rabi frequency is

$$\Omega_{n,n-1} = \sqrt{n}\eta\Omega. \quad (1.7)$$

When we set $\delta = 0$, the evolution of the states is

$$\begin{aligned} |en\rangle &\rightarrow \cos\left(\frac{\theta}{2}\right) |en\rangle - i \sin\left(\frac{\theta}{2}\right) e^{i\phi} |gn\rangle \\ |gn\rangle &\rightarrow -i \sin\left(\frac{\theta}{2}\right) e^{-i\phi} |en\rangle + \cos\left(\frac{\theta}{2}\right) |gn\rangle \end{aligned} \quad (1.8)$$



where $\theta = \Omega\tau$, with the laser pulse duration τ . By tuning the duration time and the phase offset of the laser pulse, the single-qubit rotation can be achieved.

For a two-qubit gate, we use vibration as the quantum bus to communicate two qubits. At the beginning and the end of the operation, the internal states and the motional states are desired to be disentangled. In the following subsections, we will discuss three types of the two-qubit gates.

1.3.1 Cirac-Zoller gate

The first two-qubit gate operation of ion trap was proposed by J. I. Cirac and P. Zoller in 1995 [8]. It requires the motional mode to be cooled to the ground state $|n = 0\rangle$. The scheme has three steps, as illustrated in Figure 1.4.

1. Shine a laser beam with detuning $\delta = -\nu$ on the m th ion. The laser couples $|e\rangle_m |0\rangle$ and $|g\rangle_m |1\rangle$. The evolution of the states is given by

$$\begin{aligned} |e0\rangle &\rightarrow \cos\left(\frac{\theta}{2}\right) |e0\rangle - i \sin\left(\frac{\theta}{2}\right) e^{i\phi} |g1\rangle \\ |g1\rangle &\rightarrow -i \sin\left(\frac{\theta}{2}\right) e^{-i\phi} |e0\rangle + \cos\left(\frac{\theta}{2}\right) |g1\rangle \end{aligned} \quad (1.9)$$

where $\theta = \Omega_{1,0}\tau$, with the effective Rabi frequency $\Omega_{1,0} = \eta\Omega$ (see Equation (1.7)). Setting $\phi = 0$ and $\theta = \pi$ (π -pulse), if the m th ion is at $|g\rangle_m$ initially, the state remains unchanged. If the m th ion is at $|e\rangle_m$ initially, the population is driven to $|g\rangle_m |1\rangle$ and gains a phase $-i$ (see Equation (1.9)).

2. Apply a 2π -pulse ($\theta = 2\pi$) that couples $|g\rangle_n |1\rangle$ and an auxiliary state $|a\rangle_n |0\rangle$ on the n th ion. If the n th ion is at $|e\rangle$ initially, the state remains unchanged. If the n th ion is at $|g\rangle$ initially, the state gains a phase -1 .
3. Apply again a π -pulse with $\delta = -\nu$ and $\phi = 0$ on the m th ion to take the phonon

state back to $|0\rangle$.

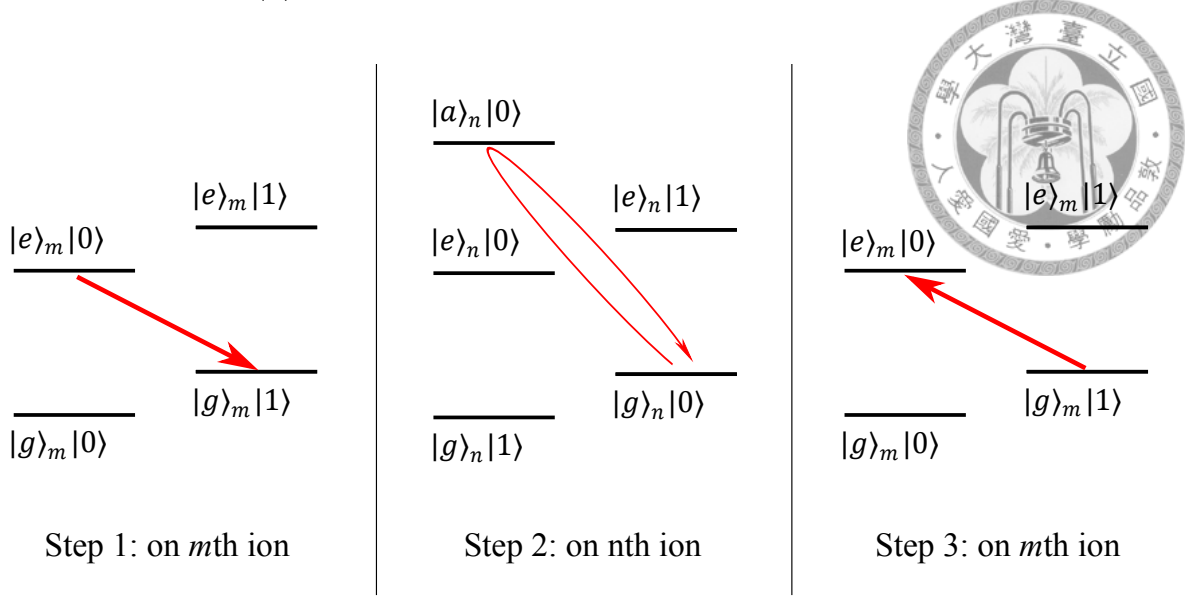


Figure 1.4: The concept of the Cirac-Zoller gate.

The overall evolution of the states then becomes

$$\begin{aligned}
 |g\rangle_m |g\rangle_n |0\rangle &\rightarrow |g\rangle_m |g\rangle_n |0\rangle \rightarrow |g\rangle_m |g\rangle_n |0\rangle \rightarrow |g\rangle_m |g\rangle_n |0\rangle \\
 |g\rangle_m |e\rangle_n |0\rangle &\rightarrow |g\rangle_m |e\rangle_n |0\rangle \rightarrow |g\rangle_m |e\rangle_n |0\rangle \rightarrow |g\rangle_m |e\rangle_n |0\rangle \\
 |e\rangle_m |g\rangle_n |0\rangle &\rightarrow -i |g\rangle_m |g\rangle_n |1\rangle \rightarrow i |g\rangle_m |g\rangle_n |1\rangle \rightarrow |e\rangle_m |g\rangle_n |0\rangle \\
 |e\rangle_m |e\rangle_n |0\rangle &\rightarrow -i |g\rangle_m |e\rangle_n |1\rangle \rightarrow -i |g\rangle_m |e\rangle_n |1\rangle \rightarrow -|e\rangle_m |e\rangle_n |0\rangle
 \end{aligned} \tag{1.10}$$

Define $|g\rangle = |0\rangle$ and $|e\rangle = |1\rangle$, then we get the CPF gate. Because the effective Rabi frequency $\Omega_{n,n-1}$ is different with different phonon state $|n\rangle$, we need to cool the motional state to the ground one $|n = 0\rangle$.

Cirac-Zoller gate was first realized by Schmit-Kaler et al. in 2003 [22].

1.3.2 Mølmer-Sørensen gate

K. Mølmer and A. Sørensen proposed the gate scheme that can be operated in thermal motion [9]. In this scheme, we apply bichromatic laser beams on both ions. The laser frequencies are $\omega_{eg} \pm \delta$, which are close to the blue and red sidebands, respectively. The energy levels and the transition paths are shown in Figure 1.5.

In the weak-field regime $\eta\Omega \ll \nu - \delta$, the phonon number n only changes by ± 1 .

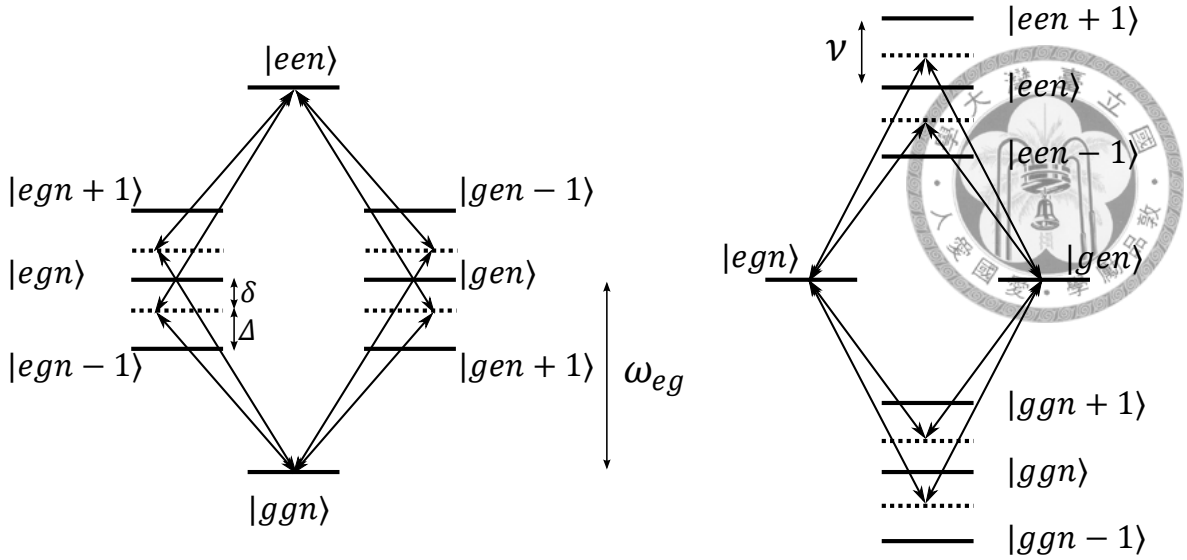


Figure 1.5: The concept of the Mølmer-Sørensen gate. Bichromatic laser beams are applied on the ions. The intermediate states are not populated because of the off resonance. The overall transitions are $|ggn\rangle \leftrightarrow |een\rangle$ (left panel) and $|egn\rangle \leftrightarrow |gen\rangle$. These paths interfere destructively and eliminate the dependence of phonon number n [10].

In the left panel of Figure 1.5, the path $|ggn\rangle \leftrightarrow \{|egn \pm 1\rangle, |gen \pm 1\rangle\} \leftrightarrow |een\rangle$ is the cascade-type Raman transition with multi intermediate levels. Since the intermediate states do not fulfill the resonance condition, these states are not populated in the process.

The evolution is then

$$\begin{aligned} |een\rangle &\rightarrow \cos\left(\frac{\tilde{\Omega}\tau}{2}\right) |een\rangle + i \sin\left(\frac{\tilde{\Omega}\tau}{2}\right) |ggn\rangle \\ |ggn\rangle &\rightarrow i \sin\left(\frac{\tilde{\Omega}\tau}{2}\right) |een\rangle + \cos\left(\frac{\tilde{\Omega}\tau}{2}\right) |ggn\rangle \end{aligned}, \quad (1.11)$$

with the effective Rabi frequency

$$\tilde{\Omega} = \sum_m \frac{\Omega_{nm}\Omega_{mn}}{\Delta_m}, \quad (1.12)$$

where m denotes the intermediate states $|eg \pm 1\rangle$ and $|ge \pm 1\rangle$, Ω_{nm} (Ω_{mn}) is the effective Rabi frequency driving $|ggn\rangle \leftrightarrow |m\rangle$ ($|m\rangle \leftrightarrow |een\rangle$) (shown in Equation (1.5) and (1.7)), and $\Delta_m = \omega_m - (E_m - E_{ggn})$ with ω_m the laser frequency driving $|ggn\rangle \leftrightarrow |m\rangle$ and $(E_m - E_{ggn})$ the energy spacing between $|m\rangle$ and $|ggn\rangle$.

We get

$$\tilde{\Omega} = \frac{\eta^2 \Omega^2}{\nu - \delta}, \quad (1.13)$$

which is independent of the phonon number n . The independence of n is because the transitions $|ggn\rangle \leftrightarrow \{|egn - 1\rangle, |gen - 1\rangle\} \leftrightarrow |een\rangle$ gives a factor of n , and the transition $|ggn\rangle \rightarrow \{|gen + 1\rangle, |egn + 1\rangle\} \leftrightarrow |een\rangle$ gives a factor of $n + 1$. These paths have opposite detunings, eliminating the dependence of n . As a result, the Mølmer-Sørensen gate can be operated when the phonon state is under thermal distribution. K. Mølmer and A. Sørensen also showed that this gate scheme has high fidelity even during heating.

Similarly, The evolution in the right panel of Figure 1.5 is

$$\begin{aligned} |gen\rangle &\rightarrow \cos\left(\frac{\tilde{\Omega}\tau}{2}\right) |gen\rangle - i \sin\left(\frac{\tilde{\Omega}\tau}{2}\right) |egn\rangle, \\ |egn\rangle &\rightarrow -i \sin\left(\frac{\tilde{\Omega}\tau}{2}\right) |gen\rangle + \cos\left(\frac{\tilde{\Omega}\tau}{2}\right) |egn\rangle \end{aligned}, \quad (1.14)$$

with the same effective Rabi frequency $\tilde{\Omega}$ shown in Equation (1.13).

Setting $\tilde{\Omega}\tau = \pi/2$, we get the maximal entanglement of the qubits. Combining with single-qubit rotation, we can achieve CNOT gate.

The experiment of the the Mølmer-Sørensen gate was first realize by C. Sackett et al. in 2000 [23]. In 2011, T. Monz et al. created 14-qubit entanglement by using this gate scheme [24].

1.3.3 Geometrical phase gate

K. Mølmer and A. Sørensen also proved that their gate scheme can be achieved without the restriction of being in the weak-field regime [10]. A similar idea was proposed independently by G. Milburn et al. in 2000 [25]. In Milburn's scheme, we apply spin-dependent forces on the ions, and drive clockwise or counterclockwise trajectories in the phase space depending on the internal states. At the end of the gate operation, the ions return to the original motional state, obtaining a phase which equals to the area of the close loop.

To study the effect of a spin-dependent force, first we consider a forced oscillator. For an oscillator with an angular frequency ν pushed by a force $F \sin \omega t$, the Hamiltonian in the interaction picture is [26]

$$H = Fx_0(ae^{i\delta t} + a^\dagger e^{-i\delta t}), \quad (1.15)$$

where $\delta = \omega - \nu$, and $x_0 = \sqrt{\hbar/(2m\nu)}$. The evolution operator of the forced oscillator is [26]

$$U(\tau) = e^{i\phi(\tau)} D(\alpha(\tau)), \quad (1.16)$$

where $D(\alpha) = e^{\alpha a^\dagger - \alpha^* a}$ is the displacement operator with $\alpha(\tau) = -\frac{i}{\hbar} \int_0^\tau F x_0 e^{i\delta t} dt$, and $\phi(\tau) = \text{Im}\{\int_0^\tau \alpha^* d\alpha\}$.

The additional phase ϕ can be understood by the relation of displacement operator $D(\alpha + \beta)e^{i\text{Im}\{\alpha^*\beta\}} = D(\alpha)D(\beta)$. Equation (1.16) can be regarded as a series of infinitesimal displacement.

After a period $\tau = 2\pi/\delta$, the displacement operator $D(\alpha) = 1$ makes the motional state back to the origin, and the state gains a phase ϕ which equals to the area of the closed loop.

For spin-dependent forces acting on the ions, the Hamiltonian is

$$H = \sum_i F x_0 (a e^{i\delta t} + a^\dagger e^{-i\delta t}) \sigma_i^z, \quad (1.17)$$

where $\sigma_i^z = |e\rangle\langle e| - |g\rangle\langle g|$ is the Pauli matrix, and the subscript $i = 1, 2$ denotes the ion's index. Equation (1.17) shows that the ion feels a force F when the internal state is $|e\rangle$, and $-F$ when the internal state is $|g\rangle$. When both ions are at the same internal states ($|ee\rangle$ or $|gg\rangle$), the ions move back and force together (center-of-mass mode). When the two ions have different internal states ($|eg\rangle$ or $|ge\rangle$), the ions move in the opposite directions (breathing mode). Consider that only the breathing mode is excited by applying the laser with frequency close to the mode frequency. If the ions' internal state is $|ee\rangle$ or $|gg\rangle$, it remains unchanged. If the ions' internal state is $|eg\rangle$ or $|ge\rangle$, the motional state displaces in the phase space.

When the ions' motional state goes back to the origin, the evolution of the internal

states is described by

$$\begin{aligned}
 |ee\rangle &\rightarrow |ee\rangle \\
 |gg\rangle &\rightarrow |gg\rangle \\
 |eg\rangle &\rightarrow e^{i\phi} |eg\rangle \\
 |ge\rangle &\rightarrow e^{i\phi} |ge\rangle
 \end{aligned}
 \tag{1.18}$$



which is illustrated in Figure 1.6. By choosing appropriate laser frequency and intensity, we can make $\phi = \pi/2$. Then Equation (1.18) is equivalent to the CFP gate up to single-qubit rotation. The experiment of the geometrical phase gate is realized by Leibried et al. in 2003 [27].

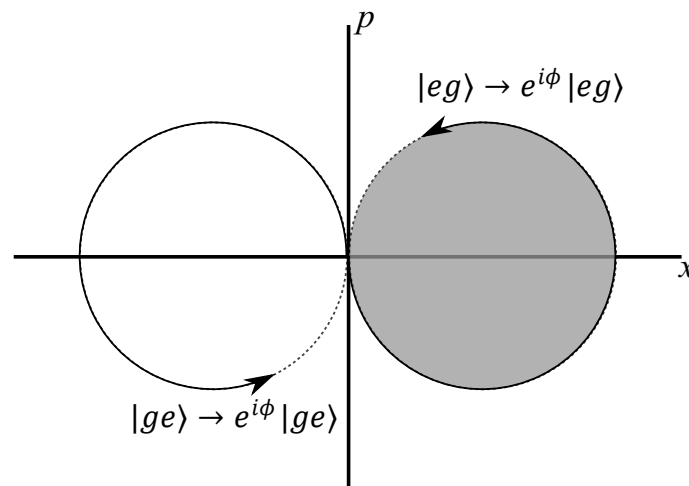


Figure 1.6: The concept of the geometrical phase gate. If the ions' internal state is $|eg\rangle$ or $|ge\rangle$, the motional state displaces in the phase space. At the end of the gate operation, the motional state goes back to the origin and gains a phase corresponding to the area of the closed loop.

1.4 Transverse-mode scheme

S.-L. Zhu and L.-M. Duan proposed to implement gates that employs the transverse motional modes instead of the traditional way with longitudinal modes [28]. The advantage of doing so is that the transverse confinement is usually much stronger than the longitudinal one so that, under the same temperature, the number of transverse phonons can be drastically suppressed, making the high-fidelity quantum gates rather robust against temperature. Further, since the transverse trapping frequency determines the highest motional

energy scale, other collective motion (longitudinal one, or dipole-dipole-like interaction from neighbors) are considered slow compared to the transverse dynamics. Therefore, every ion's transverse motion can be viewed as individual independent oscillation. This point of view allows us to consider only the local modes relevant to the participating ions in a quantum gate. A systematic way of pulse shaping was thus proposed for two-qubit gates whose speed can be made comparable to the transverse trapping frequency, which is of the order of microsecond for the gate time.

1.5 Cooling in trapped ions

In current quantum gate experiments with trapped ions, the ions are usually pre-cooled by Doppler laser cooling down to the order of millikelvin, the level so-called the Doppler temperature $T_D = \hbar\gamma/(2k_B)$, with γ the natural linewidth of the atomic state. To further go below this limit, the method of resolved sideband cooling is utilized. The idea is via the optical pumping technique by driving the red-sideband transition: Consider an trapped ion initially lies in its atomic ground state but a highly excited motional state characterized by the phonon number n . A laser beam resonant with the red-sideband transitions is applied on this ion, taking it to its atomic excited state while the phonon number is lessen by one. Next, due to spontaneous relaxation, the ion de-excites back to its ground state with the motional state of a smaller phonon number $n - 1$. By repeating such procedures, one can cool the system nearly to its ground state [29].

However, this method might not be easily generalized to large-scale ion arrays. The main obstacle is the increasing number of motional modes. A specific red-sideband laser is needed for each mode, which becomes impractical when more ions are added. In Reference [28, 30], it has been shown that the transverse-mode proposal does not require the stringent temperature requirement as the longitudinal one does. Instead, Doppler cooling suffices in the transverse scheme due to the strong confinement and hence low phonon numbers.

Such convenience does not guarantee sufficient cooling in the large-scale ion array considering the gate fidelity. The cooling issue remains with the longitudinal motion,

which still plays a role that potentially degrades the gate fidelity. The major source of error originates from the finite beam size of the control laser, for which its spatial variation of the field profile can be seen by ions moving longitudinally. In order to build a long array compatible with single ion addressability, the ion spacing must be kept nearly constant. This cannot be done by a simple harmonic trap, where the ion spacing near the trap center is squeezed every time an ion is added, unless the global axial trapping frequency is lowered accordingly. However, lower longitudinal frequency means the associated motion is more difficult to be cooled and hence more sensitive to temperature. This indeed sets a serious challenge for the large-scale ion trap quantum computation with the linear Paul trap configuration.

In this work, we propose to use optical tweezers that effectively pin some of the ions, introducing extra local traps to the system. To be more specific, we plan to apply optical tweezers used like partitions so that each “compartment” can be seen as a smaller ion trap. We will test the idea by looking mainly at the mode frequencies and the cooling efficiency.

1.6 Thesis outline

The thesis is organized as follows. In Chapter 2, we will discuss the collective motion in an ion trap. We further look at the effects of the collective motion when optical tweezers are applied regularly along the ion chain. In Chapter 3, we will discuss sympathetic cooling in the ion trap. We continuously cool some of the ions and find the temperature distribution of the ion chain, and compare the results with and without optical tweezers. We also study the relaxation dynamics of the ions as indication of cooling. Finally, we conclude our work in Chapter 4.



Chapter 2

Collective motion of trapped ions with optical tweezers

2.1 Overview

An ion trap confines N ions with the trapping frequency ω_x, ω_y , and ω_z along the x, y , and z directions, respectively. Typically, $\omega_x = \omega_y$, and $\omega_{x(y)} \gg \omega_z$ so that all the N ions are aligned along the z axis. As more ions are added in the trap, the “inner” ions are pushed closely by the “outer” ones, causing the spacing around the trap center to decrease. To keep a certain distance between ions for individual laser addressing, we need to reduce the trapping frequency ω_z as N grows. Meanwhile, it is however more difficult to cool lower frequency phonon modes. This can be seen from the estimated phonon number $\bar{n} \sim k_B T / (\hbar \omega)$. To overcome this problem, we test the idea by applying optical tweezers on the ions [15], which are arranged regularly along the chain as shown in Figure 2.1. By raising the tweezer frequency for local ions, the collective mode frequency will be enhanced by a few times. This will not only help phonon removal, but also set a frequency bound in a linear large-scale array, where the potential bottom of a traditional Paul trap is nearly flat.

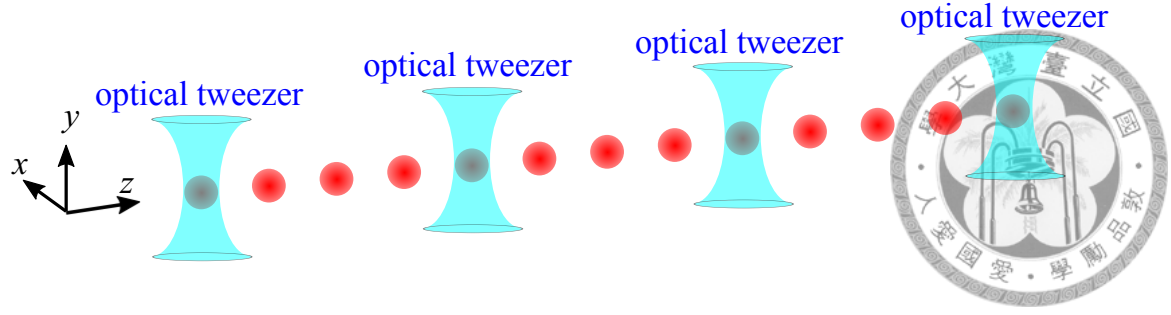


Figure 2.1: Optical tweezers are applied on the ions (nodes), who are arranged periodically on the chain.

2.2 Normal modes of the harmonic trap

For N ions in the Paul trap, the overall potential including their Coulomb interaction reads

$$U = \sum_i^N \frac{1}{2} m \omega_x^2 x_i^2 + \frac{1}{2} m \omega_y^2 y_i^2 + \frac{1}{2} m \omega_z^2 z_i^2 + \sum_i^N \sum_{j < N} \frac{e^2}{4\pi\epsilon_0} \frac{1}{|\mathbf{R}_i - \mathbf{R}_j|}, \quad (2.1)$$

where \mathbf{R}_i is the position of the i th ion. The equilibrium position z_i^0 of the i th ion can be found by solving $\partial U / \partial z_i = 0$. For convenience, we define a length unit $z_s = (\frac{e^2}{4\pi\epsilon_0 m \omega_z^2})^{1/3}$. Figure 2.2 shows the equilibrium positions of ions in units of z_s by keeping the trapping frequency ω_z fixed for $N = 1 \sim 10$.

We can see that the closest ions are at the center of the chain. The minimum spacing d_0 between ions become small as the number of ions N grows (shown in the dotted line). A numerical result of the separation of central ions as function of N is given by $d_0 \approx 2z_s N^{-0.57}$ [31], and for $N \gg 1$, $d_0 \sim z_s (\ln(N)/N^2)^{1/3}$ [32].

To find the normal modes, we do Taylor expansion around the equilibrium and get $U \approx U_0 + \sum_{\xi, \xi', i, j} \frac{1}{2} A_{ij}^{\xi\xi'} \Delta x_i^\xi \Delta x_j^{\xi'}$, where Δx_i^ξ is the displacement of the i th ion along the $\xi = x, y$ (transverse) and $\xi = z$ (longitudinal) directions with respect to its equilibrium position, and $A_{ij} = \left. \frac{\partial^2 U}{\partial x_i^\xi \partial x_j^{\xi'}} \right|_0$ ($|_0$ denotes ions at equilibrium positions) forms the coupling matrix. Here U_0 denotes the potential constant at the equilibrium but is not important. Because $x_i^0, y_i^0 = 0$, only $\left. \frac{\partial^2 U}{\partial x_i \partial x_j} \right|_0$, $\left. \frac{\partial^2 U}{\partial y_i \partial y_j} \right|_0$, and $\left. \frac{\partial^2 U}{\partial z_i \partial z_j} \right|_0$ survives. This suggests that the

motion along the x , y , and z directions is decoupled. We then have

$$A_{ij}^{\xi} = \begin{cases} m\omega_{\xi}^2 + \sum_{j=1, j \neq i}^N \frac{e^2}{4\pi\epsilon_0} \frac{a_{\xi}}{|z_i^0 - z_j^0|^3}, & i = j \\ -\frac{e^2}{4\pi\epsilon_0} \frac{a_{\xi}}{|z_i^0 - z_j^0|^3}, & i \neq j \end{cases} \quad (2.2)$$



where $a_{x(y)} = -1$ and $a_z = 2$ [28]. The mode frequencies $\omega_{\xi,k}$ and the mode functions $b_i^{\xi,k}$ of the k th mode can be found by solving the eigenvalue equation $\sum_j A_{ij}^{\xi} b_j^{\xi,k} = m\omega_{\xi,k}^2 b_i^{\xi,k}$.

The mode frequencies for $N = 1$ to 10 are shown in Figure 2.3. Here we set $\omega_{x(y)} = 10\omega_z$, and choose ω_z as the frequency unit. For the longitudinal modes (motion along the z direction), the lowest frequency corresponds to the center-of-mass mode, for which every ion moves back and forth all together. Therefore the mode frequency of this mode is exactly equal to the trapping frequency ω_z . On the contrary, for the transverse motion (along the x or y direction) the center-of-mass mode has the highest frequency. It can be observed that typically the transverse modes have higher and narrower spectral distribution than the longitudinal ones.

Though we set $\omega_{x(y)}/\omega_z$ the same value when $N = 1$ to 10 in Figure 2.3. The ratio $\omega_{x(y)}/\omega_z$ should be increased to keep the ions perfectly aligned when N gets very large. The criterion of a linear array configuration is approximated by $\omega_{x(y)}/\omega_z > 0.73N^{0.86}$ [32], and for $N \gg 1$, $\omega_{x(y)}/\omega_z > 0.77N/\sqrt{\ln N}$ [33].

2.3 Normal modes when applying optical tweezers

Optical tweezers are dipole forces that can be formed by focused Gaussian beams incident on an atom. Suppose a laser beam is incident on a target ion from the y direction, which is perpendicular to the axis of the ion chain. When the field is largely detuned, it introduces a tweezer potential

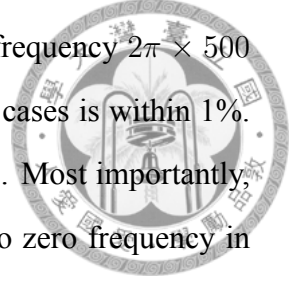
$$U = \frac{2U_0}{w_0^2}(x^2 + z^2)$$

where $U_0 = -\frac{3\gamma P}{ck^3w_0^2\delta}$ with γ the natural linewidth, $\delta < 0$ corresponding to red detuning, k , w_0 , P are the wavenumber, beam size, power of the laser, respectively. Here we ignore the y direction term because the transverse confinement of a Paul trap is typically much stronger than the axial trapping provided by a Gaussian tweezer beam along the y direction. By applying optical tweezers on some of the ions (called pinned ions), we effectively change the local frequencies experienced by the pinned ions, i.e., $\omega_{z(x),i} \rightarrow \omega_{z(x),i} = \omega_{z(x)} + \omega_{ot}$. Then we have a new matrix $A^{z(x)}$ and new eigenfrequencies $\omega_{z(x),k}$.

Figure 2.4 shows the mode frequencies of 13 ions given different numbers of optical tweezer beams. We set $\omega_x = 10\omega_z$, and choose ω_z as the frequency unit. The subfigures (a), (c), (e), and (g) correspond to the longitudinal mode, and (b), (d), (f), and (h) the transverse mode. The optical tweezers are arranged periodically. The period for pinned ions are 12, 6, 4, and 3 for the subfigure (a)(b), (c)(d), (e)(f), and (g)(h), respectively. In other words, the indices of pinned ions in the subfigure (a) and (b) are $i = 1$ and 13; $i = 1, 7$ and 13 in (c) and (d); $i = 1, 5, 9$ and 13 in (e) and (f). $i = 1, 4, 7, 10$ and 13 in (g) and (h). For a small optical tweezer frequency, the eigenfrequencies grow as ω_{ot} increases. Note that when ω_{ot} keeps increasing, the eigenfrequencies of N_p modes grows like $\omega_{z(x)} + \omega_{ot}$ where N_p denotes the number of pinned ions. The other $N - N_p$ eigenfrequencies, however, approach to fixed values in the limit of large ω_{ot} . The reason why these frequencies are bounded is that, as ω_{ot} gets large, the "pinned ions" act more like a fixed one, leaving $N - N_p$ degrees of freedom.

We calculate the lowest mode frequency ω_{low} of the ion chain with different N when applying optical tweezers regularly on one of every 10 ions. As an example, we choose $^{171}\text{Yb}^+$ ions and see how the lowest frequency scales with increasing number of ions while keeping the minimum separation $d_0 = 10 \mu\text{m}$. The result is shown in Figure 2.5. We find for a typical ion trap that contains a few tens of ions, even though the application of tweezers does raise the lowest mode frequency, its value is mainly determined by the trapping frequency. However, as more and more ions are added and the global trap gets shallower, the effect due to optical tweezers becomes more and more dominant. On the other hand, the enhancement of the lowest frequency has an upper bound as the tweezer

strength increases. Explicitly, we compare the lowest mode in the two cases of strictly fixing the end ions in space and “optical pinching” the end ions by frequency $2\pi \times 500$ kHz. We find that the deviation of the frequency between these two cases is within 1%. This suggests that the pinned ions set potential “walls” for other ions. Most importantly, it can be seen that, without tweezers, the lowest mode approaches to zero frequency in the limit of a large-scale array. The zero-frequency mode is equivalent to pure translation, and is extremely hard to be cooled for charged particles. By means of optical tweezers, the longitudinal fundamental frequencies are provided by pinned ions. This feature does not depend on the global trap and is thus scalable.



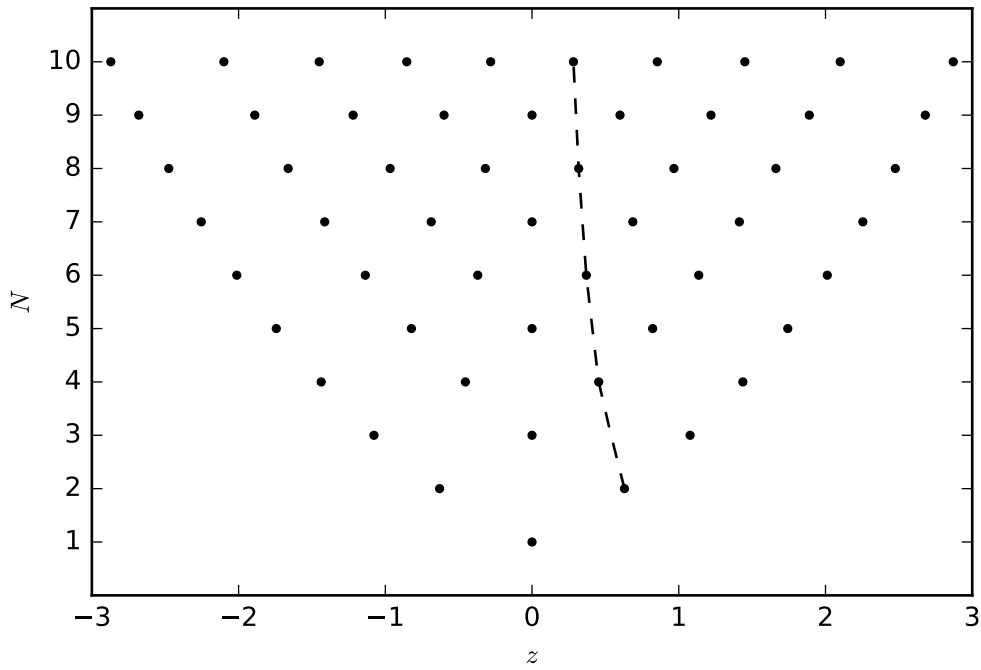


Figure 2.2: The equilibrium position of ions. The length unit is z_s . The dotted line shows the separation between central ions decreases as number of ions increases [31].

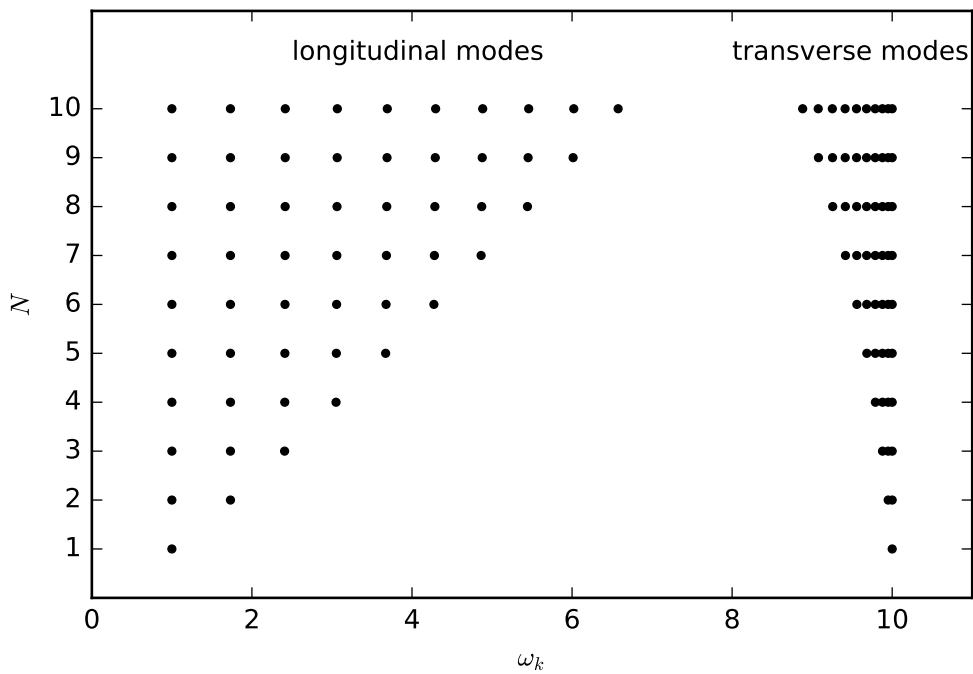


Figure 2.3: The normal mode frequencies of ions. The frequency unit is trapping frequency ω_z . $\omega_{x(y)} = 10\omega_z$.

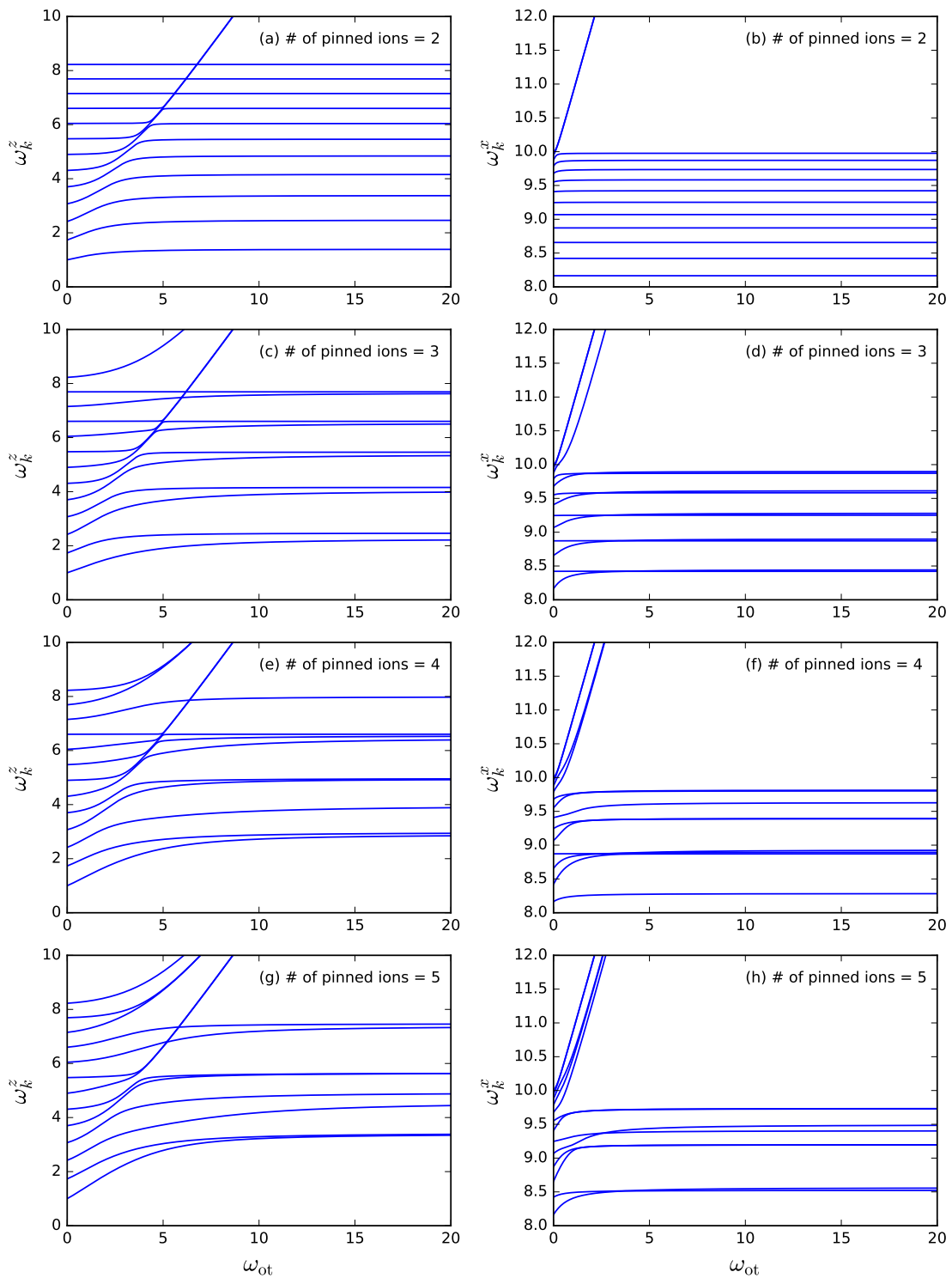


Figure 2.4: The (a)(c)(e)(g) longitudinal and (b)(d)(f)(h) transverse mode frequencies of 13 ions applied by optical tweezers periodically with the tweezers period (a)(b) 12, (c)(d) 6, (e)(f)4, and (g)(h)3.

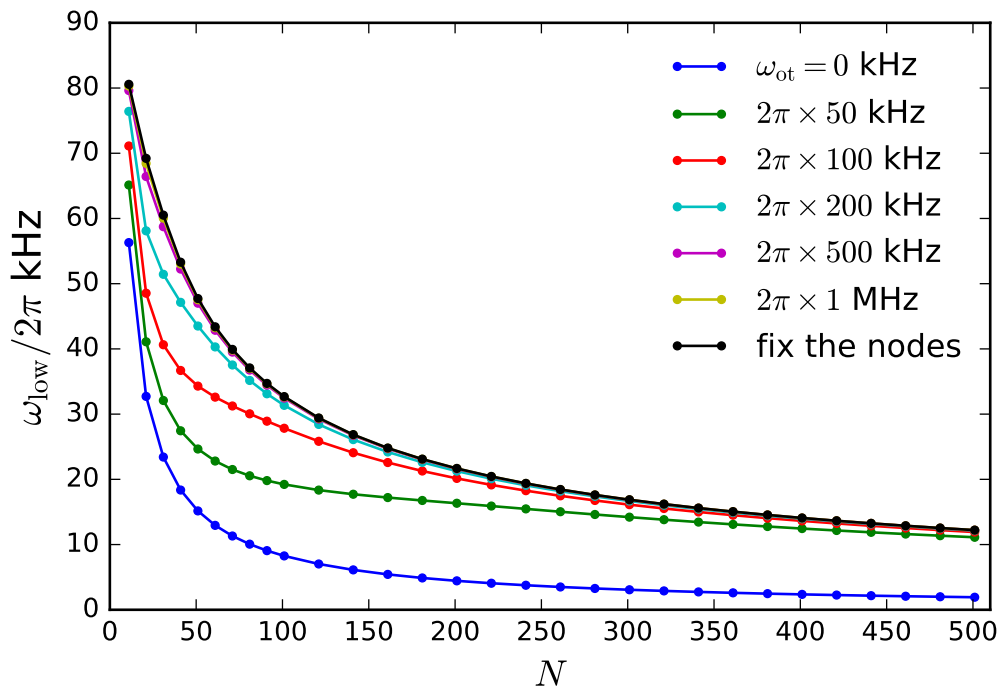


Figure 2.5: The mode frequency of the lowest mode. $^{171}\text{Yb}^+$ ions are trapped with the minimal spacing $d_0 = 10 \mu\text{m}$. We apply optical tweezers periodically on the first of every 10 ions.



Chapter 3

Sympathetic cooling for large-scale computing

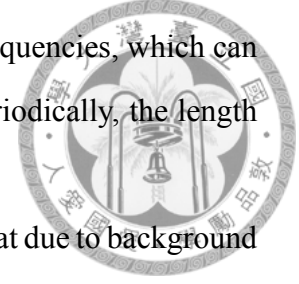
3.1 Overview

In experiments, a large chain is hard to be constructed. For an ion array of small size, the typical process is via turning on the RF trap, applying Doppler pre-cooling, and waiting for ions to enter the trap and be captured. As more ions are desired, the longitudinal confinement needs to be adjusted at the same time. Otherwise, the ion spacing decreases as the number of ions increases, causing strong Coulomb interaction that contributes to heat. On the other hand, lowering the longitudinal confinement slows down the dynamics the z direction.

To overcome the challenge of construction, we propose to assemble small ion arrays into a long one. By controlling the DC voltages that provide the longitudinal potential, one can realize many local minima each of which can be considered as a small ion trap. Similar to the ion shuttling proposal, small arrays can be moved and merged by varying the voltages. But, at this stage, ions have not yet contained quantum information. The Doppler cooling laser can be still on to stabilize the ion array.

When the length of the ion chain becomes large, the majority of ions sits at the flat bottom of the potential. Coulomb interaction from both sides cancels out as long as ions

are distributed uniformly. Under this condition, we propose to use optical tweezers that pin the ions in space. The optical tweezers provide local trapping frequencies, which can help stabilize the linear structure. By arranging optical tweezers periodically, the length of an ion array can be arbitrarily long in principle.



During computing, cooling is still an important issue. Ions will heat due to background noise which is induced by, for example, the fluctuation of voltage of the electrodes and micromotion [34]. G.-D. Lin et al. showed that a high-fidelity gate can be achieved at Doppler temperature by using the transverse-mode gate operation [28, 30]. For long-time gate processing, we should apply laser cooling continuously to maintain the ion chain at such a low temperature. However, an ion which is Doppler cooled can not participate in quantum computation because its qubit state will be destroyed repeatedly during the cooling process. The solution to this problem is via sympathetic cooling [16]. Under sympathetic cooling, a subset of ions (cooling ions) are laser cooled continuously and play the role of “heat drain”. The motional occupation of other ions (qubit ones) will decrease through heat exchange (due to Coulomb interaction) between ions (Figure 3.1). G.-D. Lin et al. showed that in principle we can cool a large ion crystal efficiently by arranging the cooling ions periodically [17].

In this chapter, we discuss the ions’ motion under sympathetic cooling associated with optical tweezers. First, we show the motional steady state of ions when arranging laser cooling and optical tweezers periodically. Then, we apply optical tweezers on just two chosen ions that contain two computational ions in between. Finally, we study the associated relaxation dynamics and find the timescale of heat equilibration.

3.2 Model

We will discuss the motion of the ions in this section. Assume that each ion couples to an individual heat bath, which depends on laser cooling or background heating. Besides the harmonics potential and the Coulomb force, a random kick due to background noise also acts on the ion. The motion of ions are described by the Heisenberg-Langevin equation

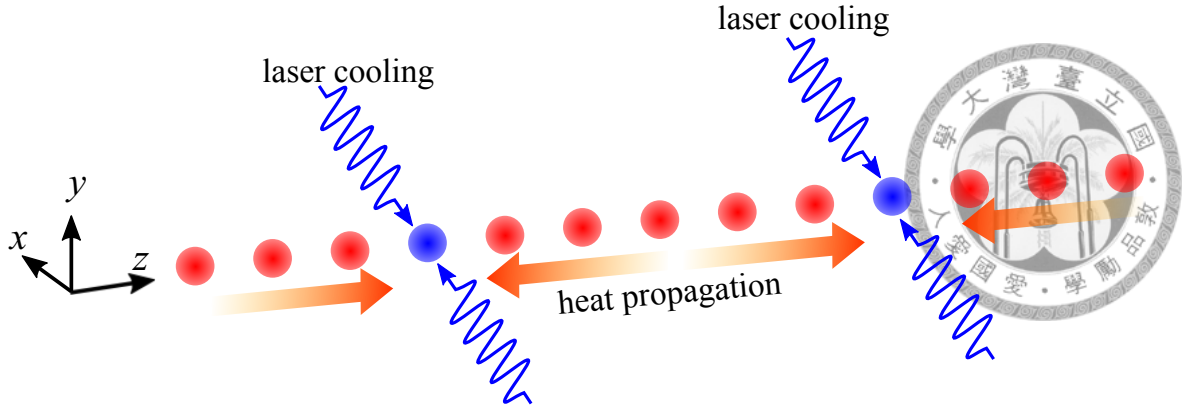


Figure 3.1: The architecture of sympathetic cooling. The cooling ions play a role of the heat drain. The computational ions will be cooled through the heat exchange due to the Coulomb interaction.

[17, 35]:

$$\begin{cases} \dot{x}_i^\xi &= p_i^\xi/m \\ \dot{p}_i^\xi &= -\sum_j A_{ij}^\xi x_j^\xi - \gamma_i^\xi p_i^\xi/m + \sqrt{2\gamma_i^\xi} \zeta_i^\xi(t), \end{cases} \quad (3.1)$$

where x_i^ξ , p_i^ξ are the i th ion's displacement and momentum operators along the longitudinal ($\xi = x$) and transverse ($\xi = y, z$) directions respectively. The elements of the matrix A^ξ are $A_{ii}^z = m\omega_{z,i}^2 + \sum_{j \neq i} \frac{e^2}{4\pi\epsilon_0} \frac{2}{|z_i^0 - z_j^0|}$, $A_{ij}^z = -\frac{e^2}{4\pi\epsilon_0} \frac{2}{|z_i^0 - z_j^0|}$, $A_{ii}^{x(y)} = m\omega_{x(y),i}^2 - \sum_{j \neq i} \frac{e^2}{4\pi\epsilon_0} \frac{1}{|z_i^0 - z_j^0|}$, and $A_{ij}^{x(y)} = \frac{e^2}{4\pi\epsilon_0} \frac{1}{|z_i^0 - z_j^0|}$, which are defined in Eq. (2.2). Because the motion of the x , y , and z are decoupled, we drop the superscription ξ for convenience. The driven rate γ_i characterizes the heat exchange due to laser cooling or the background heating. The random kick has the form $\zeta_i(t) = -i\sqrt{\frac{\hbar m \omega_k}{2}} G_{ik}(b_k - b_k^\dagger)$, where ω_k , G_{ik} are the mode frequency and the mode function of the k th mode, and b_k is the phononic field operator of the k th mode. For a Markovian bath, we have $\langle b_k^\dagger(t) b_{k'}(t') \rangle = n_k^B(T) \delta_{kk'} \delta(t-t')$, where $n_k^B(T) = 1/(\exp(\hbar\omega_k/k_B T) - 1)$ is the phonon number of the k th mode at temperature T . Therefore, the correlation of the random kick is $\langle \zeta_i(t) \zeta_j(t') \rangle = \delta_{ij} \delta(t-t') \Theta_i(T_i)$, where $\Theta_i(T_i) = \sum_k \hbar m \omega_k G_{ik}^2 (n_k^B(T_i) + \frac{1}{2})$, and T_i is the temperature of the bath of the i th ion.

Equation (3.1) can be recast into $\dot{\mathbf{q}} = -\Omega \mathbf{q} + \eta(t)$, where we define

$$\mathbf{q} \equiv (x_1, x_2, \dots, p_1/m, p_2/m \dots)^\top = \begin{pmatrix} \{x_i\} \\ \{p_i/m\} \end{pmatrix},$$

$$\eta(t) \equiv \begin{pmatrix} \{0\} \\ \{\sqrt{2\gamma_i}\zeta_i/m\} \end{pmatrix},$$

and

$$\Omega \equiv \begin{pmatrix} 0 & -I \\ [A_{ij}/m] & [\delta_{ij}\gamma_i/m] \end{pmatrix},$$



which can be diagonalized as $[U^{-1}\Omega U]_{\alpha\beta} = \lambda_\alpha\delta_{\alpha\beta}$. The formal solution to Equation (3.1)

is

$$\mathbf{q}(t) = e^{-\Omega t}\mathbf{q}(0) + \int_0^t d\tau e^{\Omega(\tau-t)}\eta(\tau).$$

Then we have the variance

$$\begin{aligned} \langle q_\mu^2(t) \rangle &= \sum_{s=1}^N \sum_{\alpha,\beta=1}^{2N} U_{\mu\alpha}U_{\mu\beta} \left(e^{-(\lambda_\alpha+\lambda_\beta)t} \left[\langle x_s^2(0) \rangle U_{\beta s}^{-1}U_{\alpha s}^{-1} \right. \right. \\ &\quad \left. \left. + \langle (p_s(0)/m)^2 \rangle U_{\beta,s+N}^{-1}U_{\alpha,s+N}^{-1} \right] \right. \\ &\quad \left. + (1 - e^{-(\lambda_\alpha+\lambda_\beta)t}) \frac{2\gamma_s\Theta_s}{\lambda_\alpha + \lambda_\beta} U_{\beta,s+N}^{-1}U_{\alpha,s+N}^{-1} \right), \end{aligned} \quad (3.2)$$

where $\mu = 1, 2, \dots, N$ represent the position, and $\mu = N + 1, N + 2, \dots, 2N$ represent the momentum. The position fluctuation of the i th ion is $\delta x_i^\xi \equiv \sqrt{\langle x_i^\xi \rangle}$. To get Equation (3.2), we have used $\langle \eta_i \rangle = 0$. The first two terms depend on initial conditions, which vanish in the long-time limit as long as $\text{Re}\{\lambda_i\} > 0$. Therefore, only the third terms survives, which is determined by the baths.

There are two major sources of computational error in ion trap based quantum computing. Here we only focus on the scheme of transverse mode quantum gate for its advantage of being insensitive to the temperature [28]. The first type of error comes from the next order correction to the Lamb-Dicke approximation. The estimated infidelity is given by [10]

$$\delta F_i^x \sim \pi^2 \eta_i^4 n_x^2 \sim \pi^2 (|\Delta\mathbf{k}|\delta x_i)^4/4, \quad (3.3)$$

where $\eta \equiv |\Delta\mathbf{k}|\sqrt{\frac{\hbar}{2m\omega_x}}$ is the Lamb-Dicke parameter with $|\Delta\mathbf{k}|$ wavevector difference of two counter-propagator laser beams, and n_x is the phonon number of the transverse mode.

The second type of error reflects the longitudinal position fluctuation so that the ion may experience non-uniformity of the laser field. Typically, a laser beam incident transversely can be approximated by $\Omega(z) \sim \Omega e^{-((z-z_i^0)/w)^2}$. The associated infidelity is [30]

$$\delta F_i^z \sim \pi^2 (\delta z_i / w)^4 / 4. \quad (3.4)$$

Note that in [30], it has been shown that with Doppler cooling, the infidelities $\delta F^z \sim 10^{-4}$ and $\delta F^x \sim 10^{-3}$ at Doppler temperature T_D . In the following, we will mainly discuss δx_i and δz_i relative to the value at T_D . From Equation (3.3) and (3.4), we know $\delta F^\xi \propto (\delta x^\xi)^4$. If δx^ξ doubles, the error is 16 times.

For convenience, we take the minimum separation of ions d_0 as the length unit, $\omega_0 \equiv \sqrt{\frac{e^2}{4\pi\epsilon_0} \frac{1}{m d_0^3}}$ as the frequency unit, and the ion's mass m as the mass unit. Throughout this chapter, we take the example of $^{171}\text{Yb}^+$ ions arranged in an array with minimum separation $10 \mu\text{m}$, so $d_0 = 10 \mu\text{m}$, $\omega_0 = 2\pi \times 143 \text{ kHz}$.

3.3 Steady state

3.3.1 Thermal equilibrium

First we consider the thermal equilibrium distribution. The whole ion chain is under a definite temperature T . From $x_i = \sum_k G_{ik} \sqrt{\frac{\hbar}{2m\omega_k}} (a_k + a_k^\dagger)$, we have $\langle x_i^2 \rangle = \sum_k G_{ik}^2 \frac{\hbar}{2m\omega_k} (2n_k + 1) = \sum_k G_{ik}^2 \frac{\hbar}{2m\omega_k} \coth\left(\frac{\hbar\omega_k}{2k_B T}\right)$. Figure 3.2 shows the position fluctuation and the corresponding infidelity of 21 ytterbium ions with $\omega_z = 2\pi \times 34 \text{ kHz}$, $\omega_x = 2\pi \times 5.1 \text{ MHz}$ under Doppler temperature $T_D = 0.5 \text{ mK}$. The position fluctuation of the longitudinal mode is about $10^{-2} d_0$, and the position fluctuation of the transverse mode is about $10^{-4} d_0$. Note that the infidelity of the longitudinal and the transverse modes are attributed to different mechanism (Equation (3.4) and (3.3) respectively). Though δz is smaller than δx about 2 orders of magnitude, the infidelities of the two directions are both about 10^{-4} .

For the transverse mode, all the ions has approximately the same fluctuation $\delta x \approx \sqrt{\frac{k_B T_D}{m\omega_x^2}}$. It shows that we can use δx_i to reflect the ‘‘local temperature’’ of a single ion.

The reason why each ion has its local temperature is that the transverse trapping frequency dominates all the energy scale. Explicitly, here we have $\omega_x \gg \omega_0 \gtrsim \omega_z$, where ω_0 characterizes the Coulomb coupling between neighboring ions. The transverse motion of a single ion is hard to be affected by the other ions so the transverse position fluctuation is mainly determined by its local temperature. On the contrary, since the Coulomb coupling is comparable to or even larger than the longitudinal characteristic energy, the position fluctuation for the longitudinal mode depends on the ions more collectively and therefore the longitudinal one is called the “soft mode.”

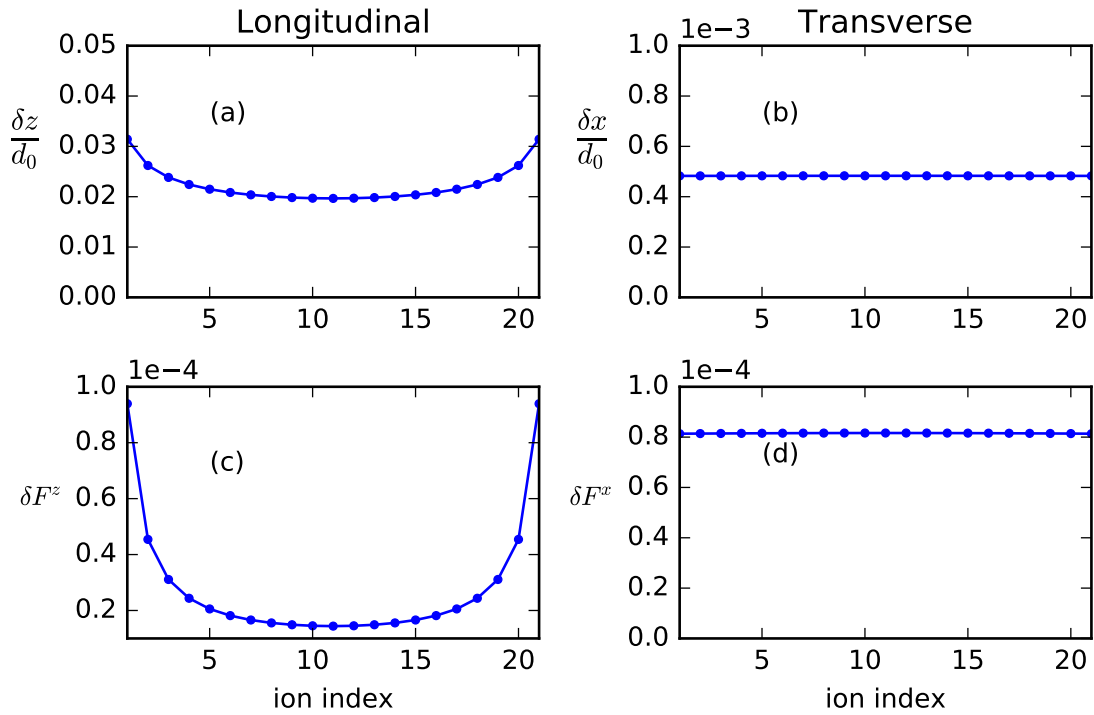


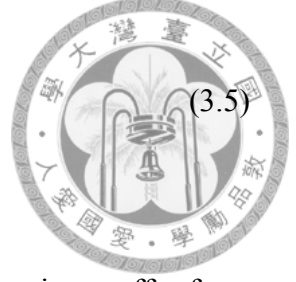
Figure 3.2: (a)(b)The position fluctuation and (c)(d) its corresponding infidelity of 21 $^{171}\text{Yb}^+$ ions with minimum separation $d_0 = 10 \mu\text{m}$ under Doppler temperature $T_D = 0.5 \text{ mK}$. ($k_B T_D / \hbar = 2\pi \times 10 \text{ Mhz} = 70\omega_0$.) Other parameters: $\omega_z = 2\pi \times 34 \text{ kHz} = 0.24\omega_0$, $\omega_x = 5.1 \text{ MHz} = 35.7\omega_0$, $|\Delta\mathbf{k}|d_0 = 157$, and $w = 0.25d_0$ [17].

3.3.2 Sympathetic cooling

Now we discuss the steady-state profile of each ion that connects to an individual heat bath. The steady state position fluctuation of the μ th ion is given by Equation (3.2) when $t \rightarrow \infty$. Since usually all the eigenvalues $\lambda_{\alpha(\beta)}$ have positive real parts, the exponential

terms vanish. The variation of the steady state becomes

$$\langle q_\mu^2 \rangle = \sum_{s=1}^N \sum_{\alpha,\beta=1}^N U_{\mu\alpha} U_{\mu\beta} \frac{2\gamma_s \Theta_s}{\lambda_\alpha + \lambda_\beta} U_{\beta,s+N}^{-1} U_{\alpha,s+N}^{-1}, \quad (3.5)$$



which is independent of the initial condition $\langle x_s^2(0) \rangle$ and $\langle p_s^2(0) \rangle$.

Here, we have a subset of ions continuously cooled, and the other ions suffer from heating from the background. We assume that, for the cooling ions, the bath temperature T_i and the driven rate γ_i are determined by Doppler laser cooling parameters. For the heating ions, we use the background phonon heating rate to characterize the driven rate γ_{bg} and the background temperature T_{bg} . The phonon heating rate of the k th mode is estimated by $\gamma_{\text{bg}} n_k^B \sim \gamma_{\text{bg}} \frac{k_B T_{\text{bg}}}{\hbar \omega_k}$. To simplify the discussion, we assume that the phonon generation rates are almost the same around all the motional modes. This rate does not individually depend on temperature. Instead, it is then characterized by the product $\kappa = \gamma_{\text{bg}} T_{\text{bg}}$. For a given κ , we have the freedom to vary T_{bg} and hence γ_{bg} accordingly.

Consider 21 ions with 5 ions on the both ends cooled continuously. Denote the set of cooling ions by C and heating ions by H . We set $T_i = T_D, \gamma = 0.1$ for $i \in C$ and $T_i = T_{\text{bg}}, \gamma_i = \kappa/T_{\text{bg}}$ for $i \in H$. The steady-state position fluctuation profiles under different background temperatures are shown in Figure 3.3. We set $\kappa = 0.01\hbar/k_B$. The red dotted line shows the ideal case which corresponds to the thermal equilibrium profile under T_D . We can see that as the background temperature increases, the position fluctuation profile of the heating ions grows, but converges to an upper bound. It gives the worst case of the infidelity. In the following discussion, we will discuss the “worst-case scenario” profile by taking $T_{\text{bg}} = 10^6 T_D$ and $\gamma_{\text{bg}} = 10^{-10} \omega_0$, which is extremely unrealistic but sets an upper bound to realistic situations.

When more ions are included in the trap, we can arrange the cooling ions periodically to cool the ion chain efficiently. Figure 3.4 shows the steady-state position fluctuation of 121 ions under periodic sympathetic cooling. We apply laser cooling continuously on the first of every 10 ions, i.e., the cooling ions are the 1st, 11th, ..., and 121st ones. For the longitudinal mode, the position fluctuation profile is almost identical to the ideal

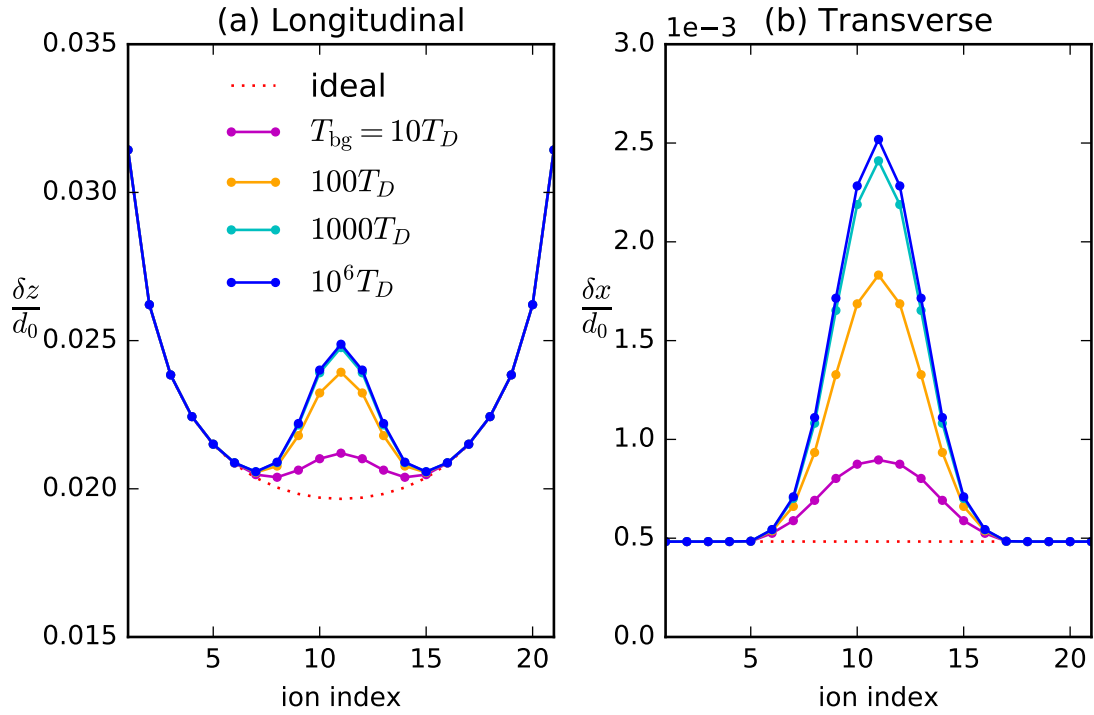


Figure 3.3: The steady state profile of 21 ions under sympathetic cooling with different background temperature. 5 ions on the both ends are cooled continuously. The ideal case corresponds to the thermal equilibrium profile under T_D . $\omega_z = 0.24\omega_0$, $\omega_x = 36\omega_0$ [17].

case. However, for the transverse mode, the position fluctuations of the heating ions are larger than the ideal case. Again, it shows that the longitudinal mode is more collective so that the heat exchange is easier to be accomplished. But the transverse mode is not. The maximum fluctuation of the transverse mode appears in the segments on the both ends of the ion array. The maximum fluctuation is about 2.1 times compared to the ideal case and gives about ~ 20 times of the infidelity. If we discard the end segments, δx_i for $i = 12$ to 110 is no more than 1.2 times of δx_i for the ideal case. The infidelity is only about 2 times larger than the ideal case.

3.4 Steady state profile with optical tweezers

3.4.1 Longitudinal modes for periodic arrangement of tweezers

As the number of ions increases, the trapping frequency ω_z should decrease to keep the ions' spacing a constant. As a result, the position fluctuation of the longitudinal direction

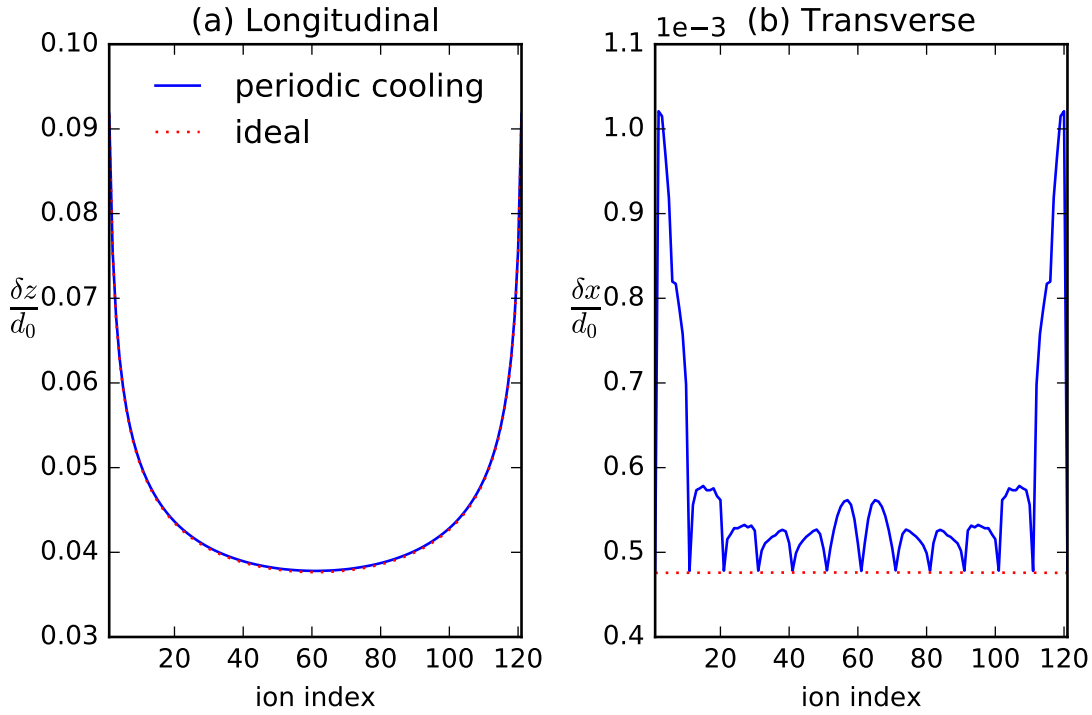


Figure 3.4: The steady profile of 121 ions under periodic sympathetic cooling. The index of the cooling ions are $i = 1, 11, \dots, 121$. For $i \in C$, $\gamma_i = 0.1\omega_0$, $T_i = T_D$. For $i \in H$, $\gamma_{bg} = 10^{-10}\omega_0$, $T_{bg} = 10^6 T_D$. $\omega_z = 2\pi \times 7.2$ kHz = $0.05\omega_0$, $\omega_x = 2\pi \times 5.1$ MHz = $36\omega_0$ [17].

grows rapidly and cause larger infidelity. We apply optical tweezers on the cooling ions to “pin” these node ions. The other ions’ fluctuation will decrease through the collective motion.

Consider the 121 ions under sympathetic cooling with cooling ions arranged periodically with a period of 10 ions. Now we apply optical tweezers of frequency $\omega_{ot} = 2\pi \times 200$ kHz also on the cooling ions. The position fluctuation profiles are plotted in Figure 3.5. The green line shows δz when we apply the optical tweezers, and the magenta dotted line shows the ideal profile. We can see that the steady-state profile can also reach the ideal case when we turn on the optical tweezers, and the values of δz_i are decreased by 1/2 compared to turning off the tweezers.

To scale up the ion trap quantum computer, we apply laser cooling and the optical tweezers regularly every 10 ions for large N . We use the average of δz of the computation ions to quantify the efficient of cooling. Define $\delta z_{avg} \equiv \frac{1}{n(H)} \sum_i \delta z_i$ for $11 < i < N - 10$ and $i \in H$, where $n(H)$ is the number of the heating ions. We plot δz_{avg} versus N around

the range $N = 11$ to 401 in Figure 3.6. When we turn on the optical tweezers, the curve increases slowly as N gets larger. It shows that applying optical tweezers can improve the stability of the longitudinal mode of the ion chain.

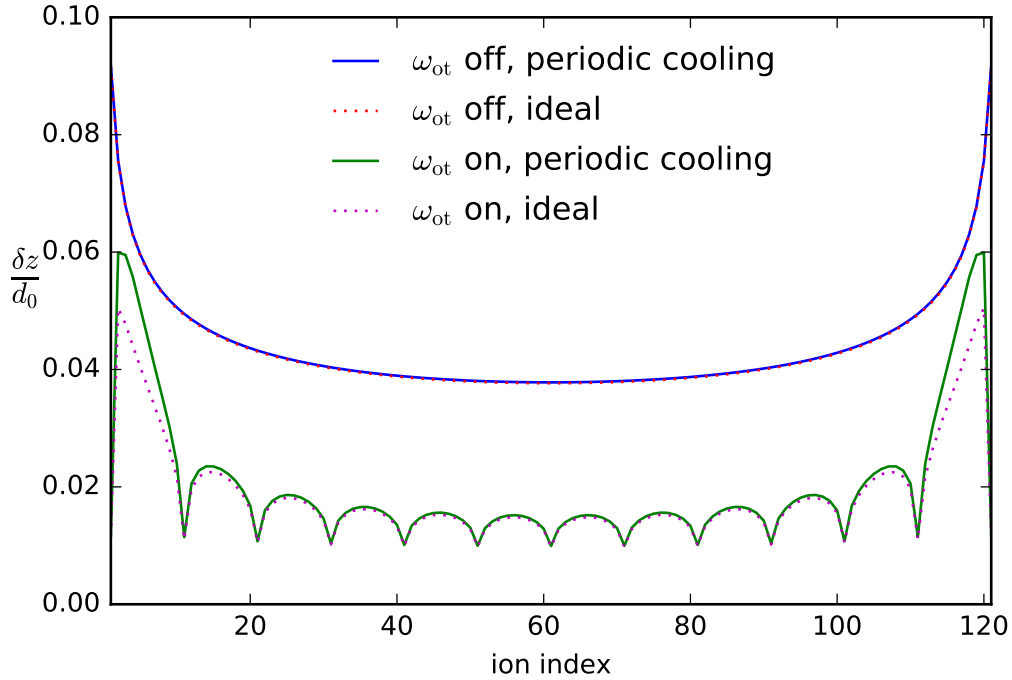


Figure 3.5: The position fluctuation of longitudinal mode under sympathetic cooling associated with optical tweezers. Blue curve: applying laser cooling on one of 10 ions. Red dotted curve: all the ions are under T_D . Green curve: applying laser cooling associated with optical tweezers with $\omega_{ot} = 2\pi \times 200 \text{ kHz} = 1.4\omega_0$ on one of every 10 ions. Magenta dotted curve: applying optical tweezers on one of every 10 ions while all of ions are under T_D . Other parameters are same as Figure 3.4.

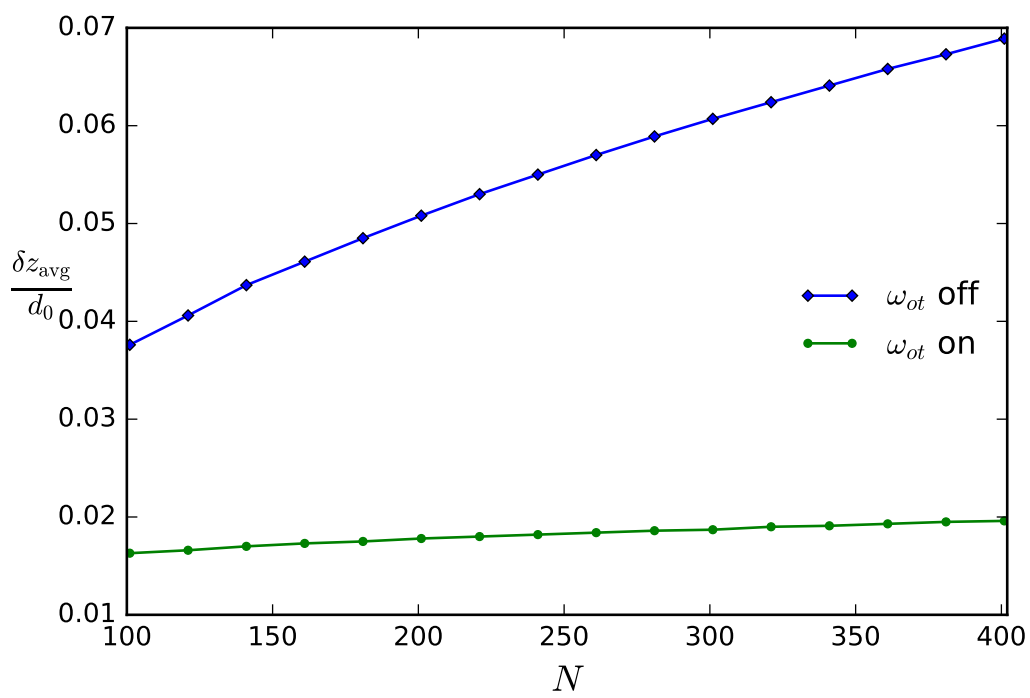


Figure 3.6: The average of position fluctuation δz_{avg} versus the ion number N . We make the minimum separation of ions $d_0 = 10 \mu\text{m}$ for every N .

3.4.2 Transverse mode for periodic arrangement of tweezers

Now we also examine the effect of optical tweezers on the transverse mode although it is, relatively speaking, not relevant since the tweezer frequency is comparable to the transverse one.

Once again, we cool the 121-ion array by arranging the cooling ions periodically with a period of 10 ions. We apply the optical tweezers on the cooling ions with the frequency $\omega_{ot} = 2\pi \times 200$ kHz in the x -direction now. Figure 3.7 shows the position fluctuation δx . Surprisingly, when we turn on the optical tweezers, δx_i for $i \in H$ are 10 to 20 times of δx_i when turning off the optical tweezers. Unlike the longitudinal mode, the efficiency get worse when we apply the optical tweezers on the transverse direction.

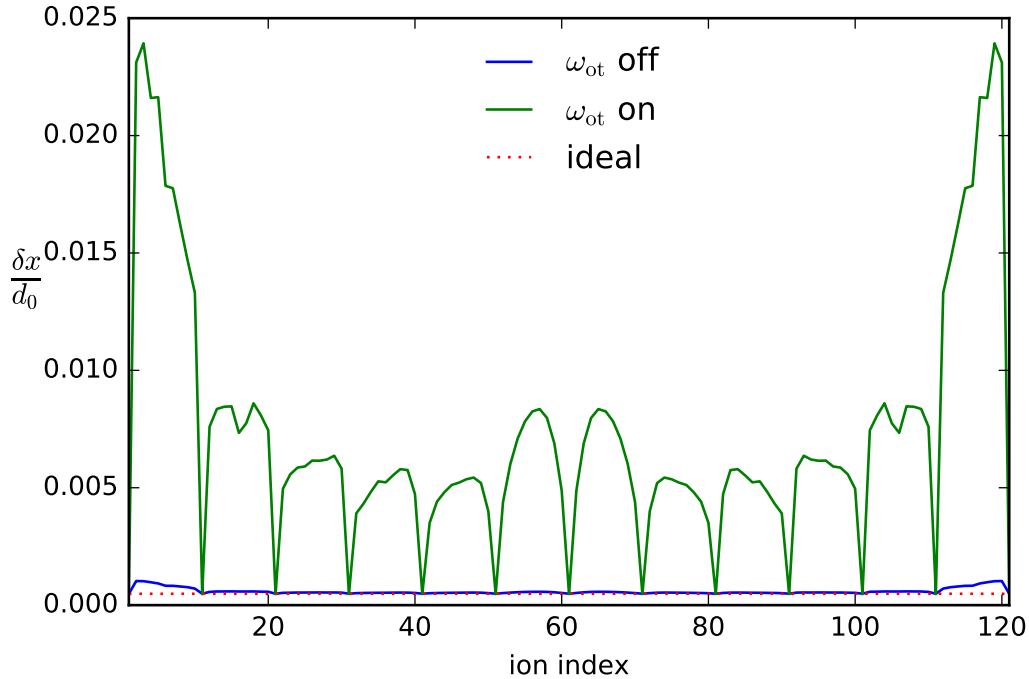


Figure 3.7: The position fluctuation of transverse mode under sympathetic cooling associated with optical tweezers. We can see that the ions have large position fluctuation when we turn the optical tweezers. Blue curve: applying laser cooling on one of 10 ions. Red dotted curve: all the ions are under T_D . Green curve: applying laser cooling associated with optical tweezers with on one of every 10 ions. The parameters are same as Figure 3.5.

The reason why the efficiency is worse when we apply the tweezers on the x direction is as follows. By considering the transverse mode only, we can treat the ions as an array

of oscillators. Every oscillator has weak coupling with each other. If the frequency of one oscillator is off resonant to the next one, they can hardly exchange energy. As a result, the optical tweezers play a role of the “heat block.” We call the ion applied by the optical tweezers “pinned ion” in the following discussion. If we cool the pinned ion, heat cannot be dissipated through the heat drain efficiently. Hence we have worse cooling efficiency.

To verify this argument, we apply the optical tweezers on heating ions rather than the cooling ions, and see the position fluctuations δx . Figure 3.8 shows δx when we still cool $i = 1, 11, \dots, 121$ ions and apply the optical tweezers on $i = 23, 49, 69, 87$ (marked by the cross symbol). We can see that those pinned ions have significant large δx , and other ions' position fluctuations are approximately same as the no-tweezers case (shown in the inset).

In Figure 3.9(a), we still cool $i = 1, 11, \dots, 121$, and pin $i = 42, 50, 92$, and 100 ions. For $i = 42$ to 50, and $i = 92$ to 100, δx_i forms a hump while other ions have approximately same δx as no-tweezers case. This is because there are no heat drain in these two segments, and the ends segments are blocked by the pinned ions. The segments cannot be cooled well.

In contrast, we can arrange the pinned ion outside the cooling ion. In Figure 3.9(b), we pin the ion for $i = 41, 51, 91, 101$ (marked by the cross symbol), and cool the ion on $i = 42, 50, 92, 100$ (marked by the cyan diamond). The segment $i = 42$ to 50 and $i = 92$ to 100 can be cooled well, and the other ions have large position fluctuations compared with the no-tweezers case. Again, it shows that pinned ion blocks the heat propagation. The segment with cooling ions on the both end has small position fluctuation. It justifies the idea of a “local trap,” which will be discussed in the next section.

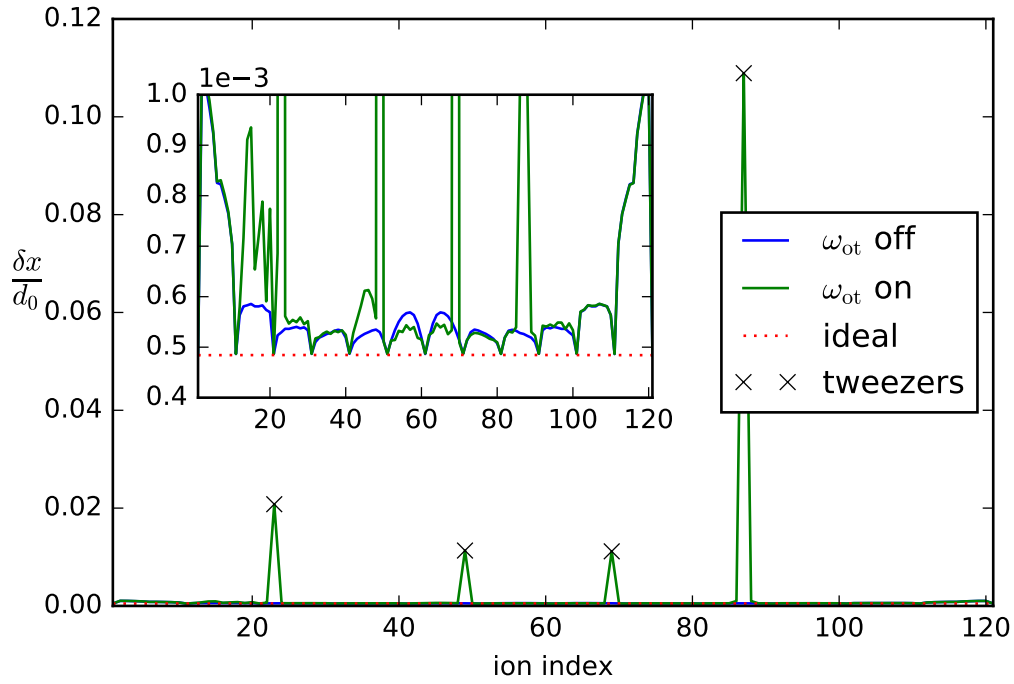


Figure 3.8: The position fluctuation of transverse mode under sympathetic cooling. The optical tweezers are applied on the heating ions. Cooling ions: $i = 1, 11, \dots, 121$. Pinned ions: $i = 23, 49, 69, 87$. The other parameters are same as Figure 3.5

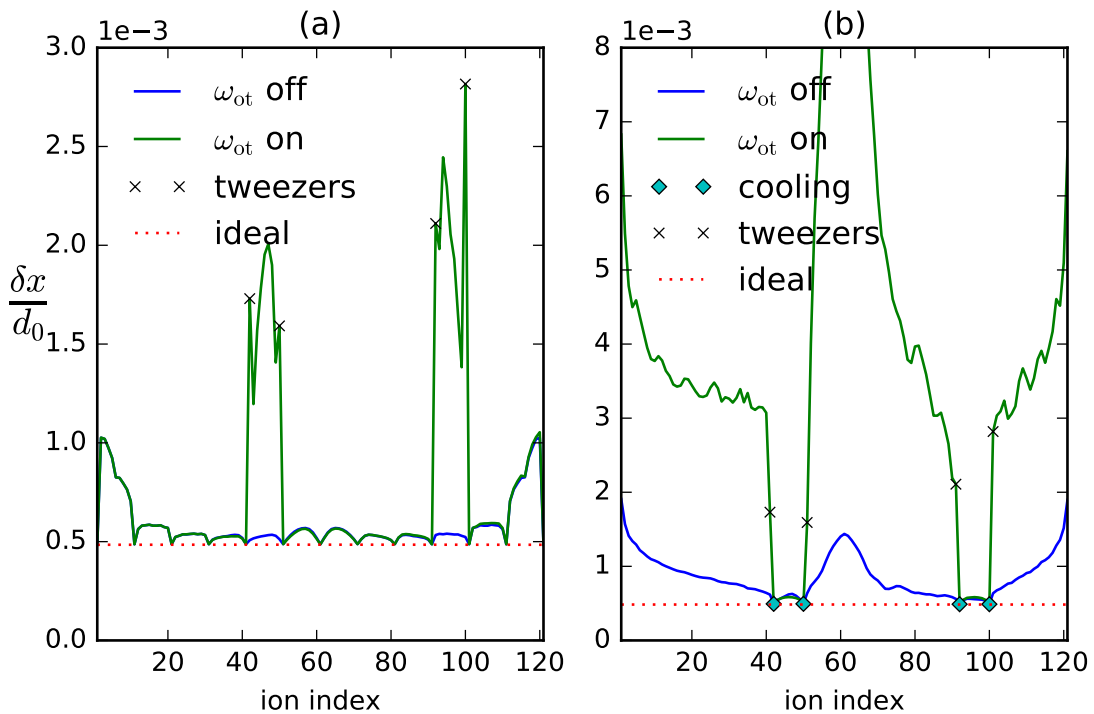


Figure 3.9: The position fluctuation of the transverse mode. (a)Cooling ions: $i = 1, 11, \dots, 121$. Pinned ions: $i = 42, 50, 92, 100$. (b)Cooling ions: $i = 42, 50, 92, 100$. Pinned ions: $i = 41, 51, 91, 101$. The other parameters are same as Figure 3.5

3.5 Local trap

In the previous discussion, we arrange the cooling ions and pinned ions periodically along the ion chain. It requires lots of laser beams. It can be expected that, if the ions that get involved in the quantum gate operations are in a local segment defined by two sets of optical tweezers, we need to just cool that segment by applying sympathetic cooling within the segment (Figure 3.10). Further, the longitudinal position fluctuation δz will be reduced because of the enhancement of the eigen-mode frequency. The pinned ions effectively blocked the heat exchange so that the fluctuations outside this segment have insignificant contributions.

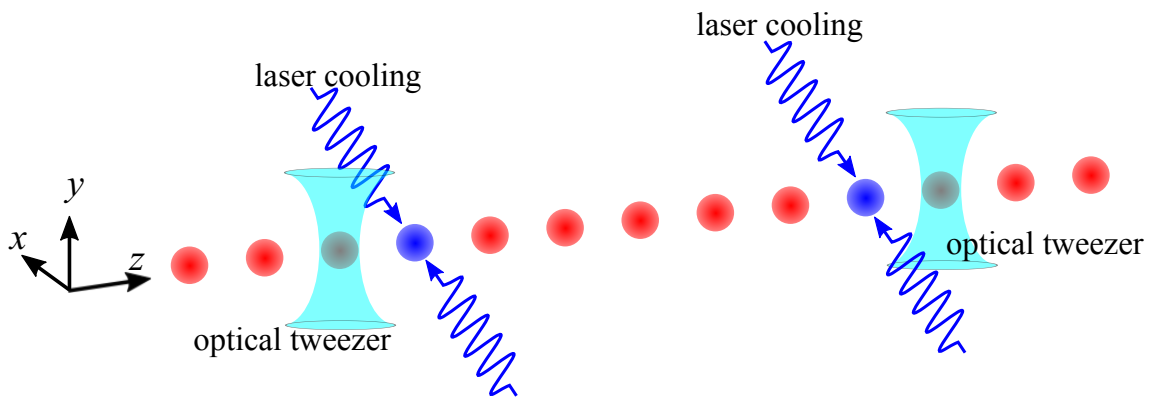


Figure 3.10: The setup of the local trap.

In Figure 3.11, we cool the 31st and 41st ion. We can see that the computational ions ($i = 32$ to 40) have smaller position fluctuations compared to the other heating ions. For the longitudinal mode, δz_i for $i = 32$ to 40 are approximately 1.04 times compared to δz_i under periodic cooling with a period of 10 ions. When we apply the optical tweezers on 30th and 42nd ions, δz_i gets much smaller. For transverse mode, the efficiency of turning on or off the optical tweezers are roughly the same. The average of position fluctuation δx_{avg} for $i = 32$ to 40 is 1.1 (1.2) when we turn off (on) the optical tweezers.

Figure 3.12 shows the position fluctuations profile of the local traps for $N = 121$. Each subfigure shows we apply laser cooling and optical tweezers on the different ions. The cooling ions are marked as the cyan diamond symbols, and the pinned ions are marked as the cross symbols. For the longitudinal mode, pinning the ions reduces the position fluctuation. The efficiency is even better compared to the periodic cooling without optical

tweezers. For the transverse mode, the efficiency depends on the cooling ions' positions.

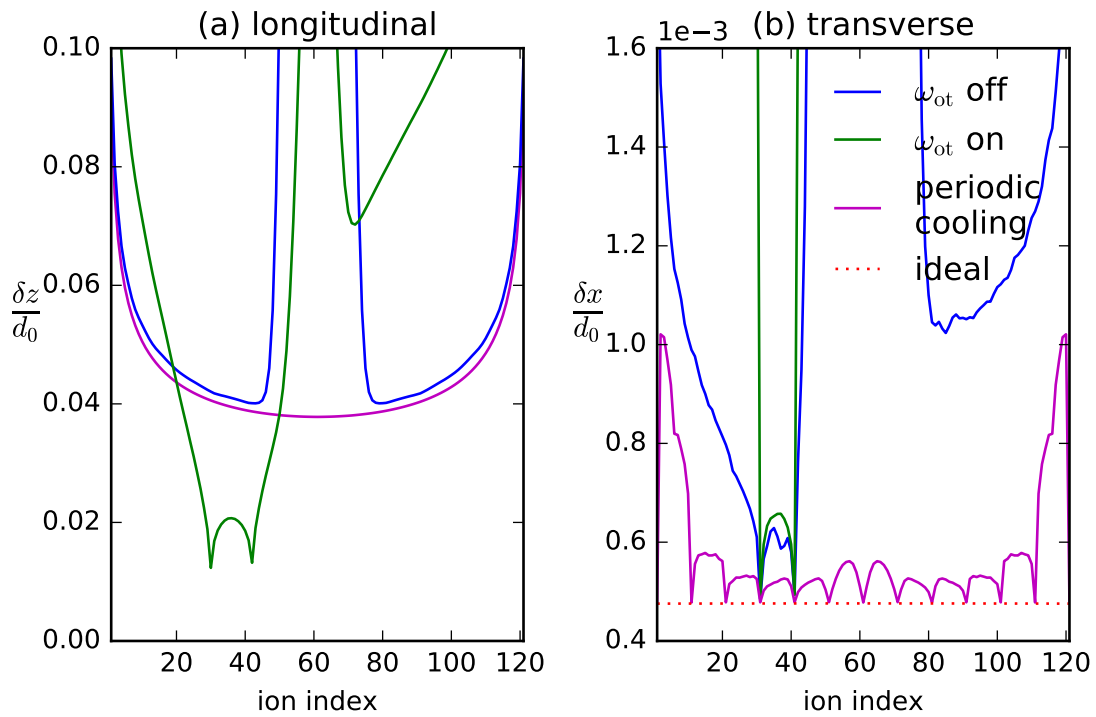


Figure 3.11: The position fluctuations of (a) longitudinal and (b) transverse mode. Blue curve: applying laser cooling on the 31st and the 41st ions. Green curve: applying laser cooling on the 31st and the 41st ions and applying optical tweezers on 30th and 42nd ions. Magenta curve: applying laser cooling on one of every 10 ions. Red dotted line: every ion is under T_D . The other parameters are same as Figure 3.5.

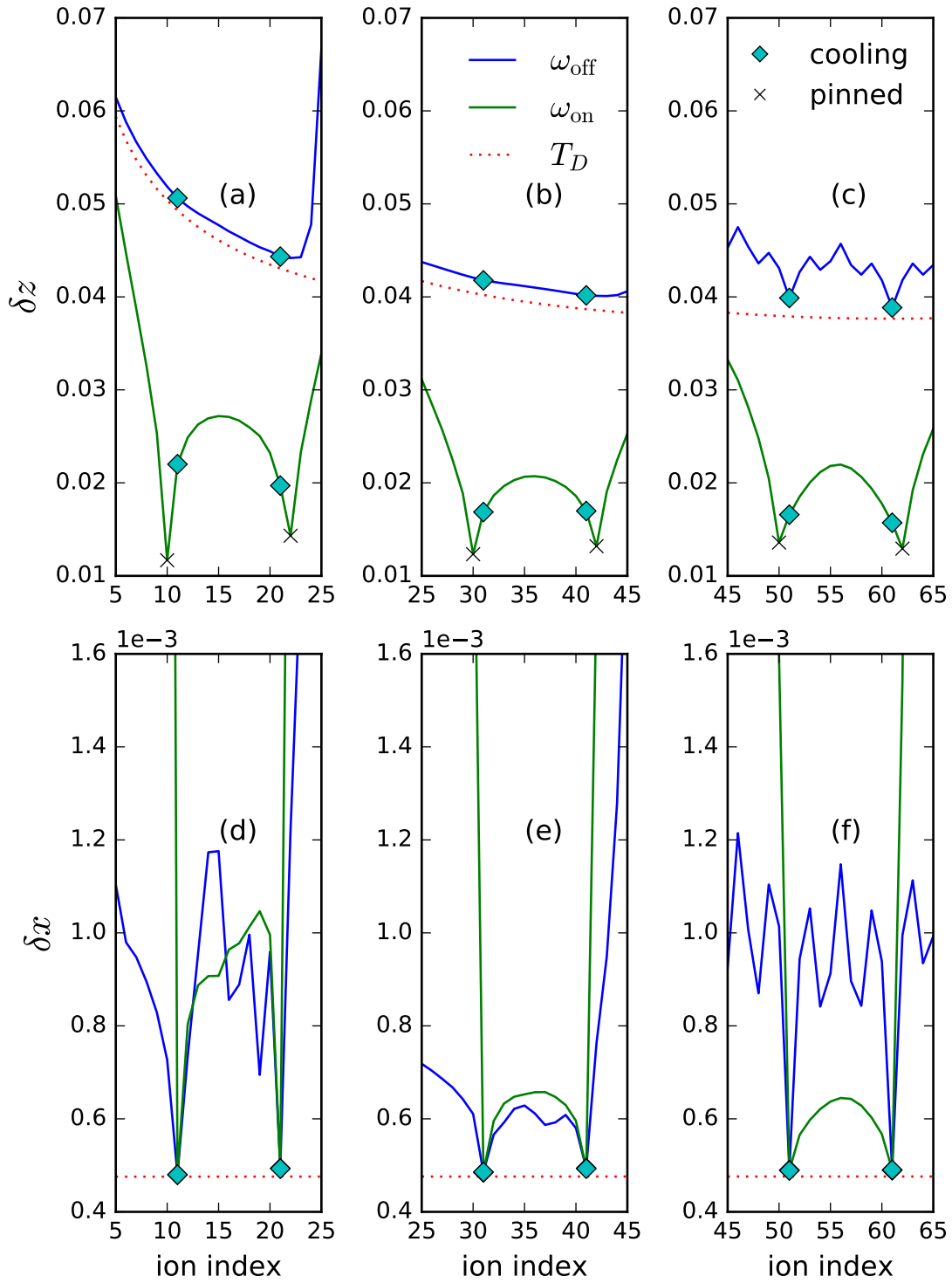


Figure 3.12: The position fluctuation profile of the local trap for $N = 121$. (a)(b)(c): Longitudinal mode. (d)(e)(f): Transverse mode. (a)(d): cooling ions: $i = 11, 21$, pinned ions: $i = 10, 22$. (b)(e): cooling ions: $i = 31, 41$, pinned ions: $i = 30, 42$. (c)(f): cooling ions: $i = 51, 61$, pinned ions: $i = 50, 62$. Blue curve: Turn off the optical tweezers. Green curve: Turn on the optical tweezers. Red curve: every ion is under T_D without the tweezers. The parameters are same as Figure 3.5.

3.6 Relaxation dynamics

In this section, we will discuss the relaxation dynamic of the local trap. We plot the time evolution of δz_i and δx_i in Figure 3.13. We take the time unit $t_0 \equiv 2\pi/\omega_0$ ($\sim 7\mu\text{s}$). We set all the ions under $10T_D$ initially without the optical tweezers. At $t = 0$, we turn on the laser cooling on the cooling ions and turn on the optical tweezers on the pinning ions. Every subfigure shows applying laser cooling on different ions. The solid curves show the time evolution of δz_i (δx_i) without the tweezers, and the dashed curves show the evolution when we turn the optical tweezers. For both longitudinal and transverse mode, it is faster to cool the ions when we apply the optical tweezers.

For the longitudinal mode, we take coarse-grain average by time interval $10t_0$ because δz_i oscillates rapidly. In Figure 3.13(a), (b), and (c), it takes about 10^4t_0 , $5000t_0$, and $8000t_0$ to reach the steady state δz^{st} when we turn off the tweezers. When the tweezers are turned on, it takes only $500t_0$, $700t_0$ and $700t_0$ to reach the same δz^{st} . The cooling time is shorter by few times to one order of magnitude when we apply the optical tweezers. The cooling time when we turn on the tweezers is less than $1000t_0 \sim 1$ ms.

For the transverse mode, $\delta x(t)$ can be smaller than the steady state δx^{st} during the cooling process. In Figure 3.13(d), (e), and (f), it takes about 2×10^4t_0 , 6×10^4t_0 , and $7000t_0$ to reach the minimum δx when the tweezers are turned off. When we turn the tweezers, it takes only 10^4t_0 , $7000t_0$, and $5000t_0$ to reach the minimum δx , which are faster than the no-tweezers case.

3.7 Gate design

In this section, we demonstrate the how to construct a CFP gate in the ion traps by using the method proposed by S.-L. Zhu et al. [36]. We chop the spin-dependent laser pulse into 9 time segments to maximize the fidelity of the computation. In Figure 3.14, we cool $i = 51$ and 61 , and apply the tweezers on $i = 50$ and 62 on the x -direction. The gate ions are $i = 55$ and 57 . Figure 3.14(a) shows the maximum fidelity with the different gate time and the laser frequency. Figure 3.14(b) shows the laser pulse shape when the gate time

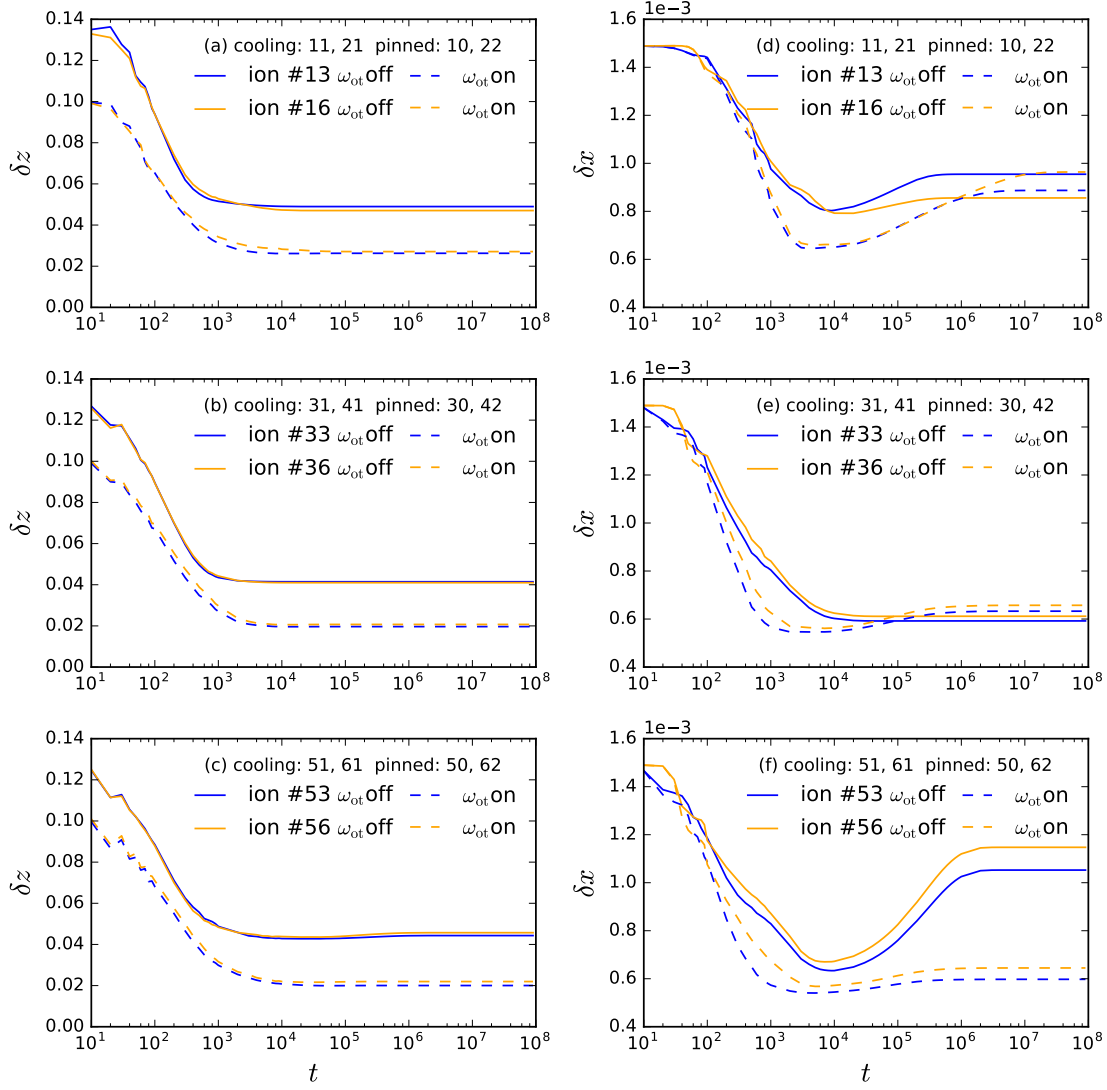


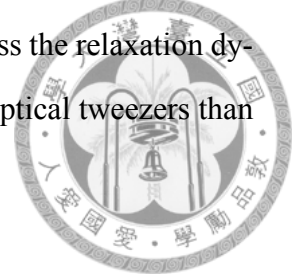
Figure 3.13: The time evolution of δz_i (a)(b)(c) and δx_i (d)(e)(f) for different segments of local traps. The cooling and pinned ions of each subfigure are same as Figure 3.12. The ion chain is under $T = 10T_D$ at $t = 0$. The other parameters are same as Figure 3.5.

$\tau = 500 \times \tau_0$ ($\tau_0 \equiv 2\pi/\omega_x$) and the laser frequency $\mu = 0.982\omega_x$ (marked by the arrow in Figure 3.14(a)). The infidelity is only 10^{-13} .

3.8 Chapter summary

To sum up, we calculate the position fluctuation of the ions as indication of cooling efficiency under sympathetic cooling together with optical tweezers. We find that for longitudinal mode, the optical tweezers together with sympathetic cooling significantly improve the cooling efficiency. For transverse mode, the optical tweezers play the role of the “heat

block”. We show that for the local gate operation, we only need to cool the ions near computational ions rather than the whole ion chain. Finally, we discuss the relaxation dynamics. We find that the cooling time is shorter when we apply the optical tweezers than that when we do not.



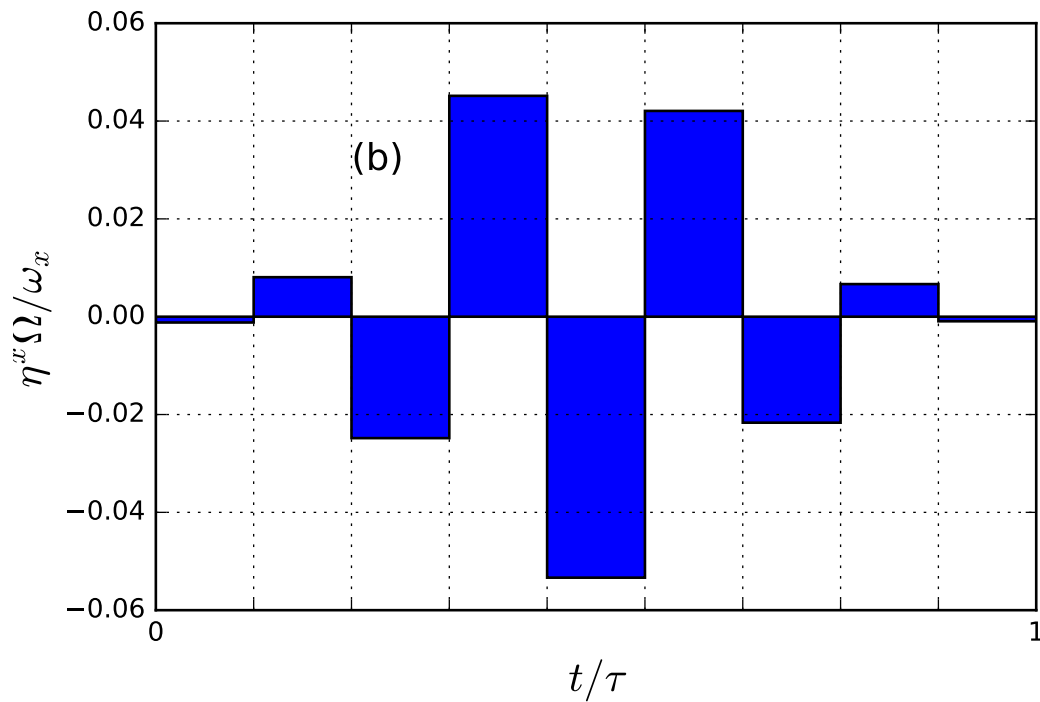
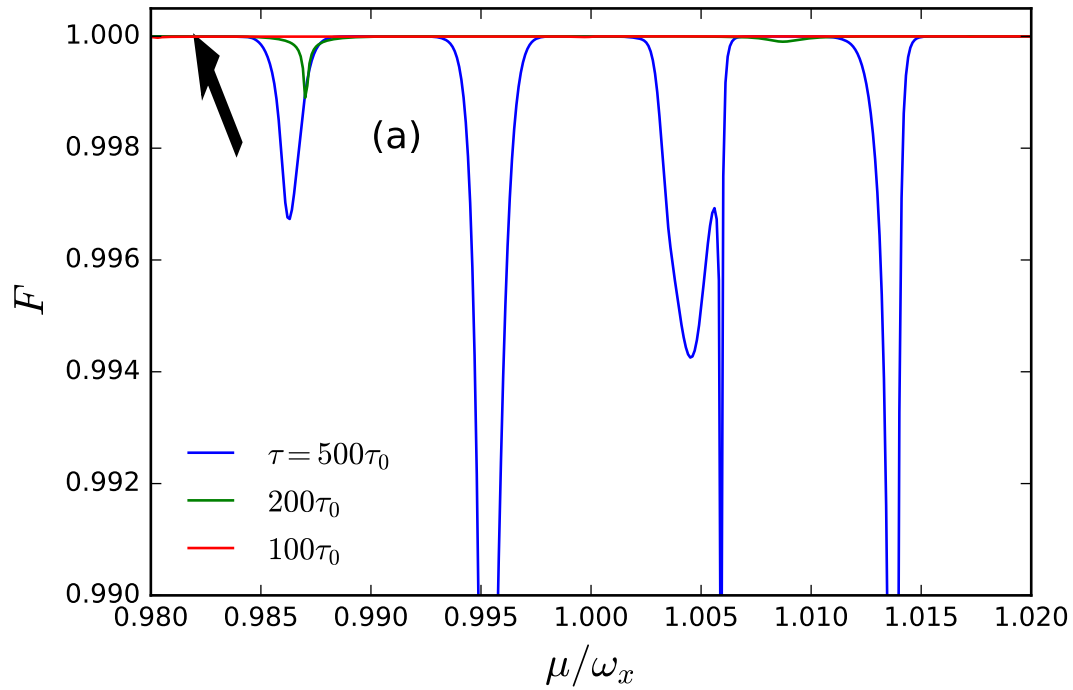


Figure 3.14: Quantum gate design for $N = 121$. Cooling ions: 51, 61. Pinned ions: 50, 62. Gate ions: 55, 57. (a) The fidelity with different gate time and laser frequency. (b) The laser shape with $\tau = 500\tau_0$ and $\mu = 0.982\omega_x$ (denoted by the arrow in (a)). $\delta F = 10^{-13}$. The other parameters are same as Figure 3.5.



Chapter 4

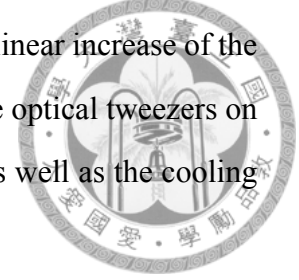
Conclusion

In this thesis, we propose a scalable ion trap quantum computer scheme. We use optical tweezers to stabilize the ion chain, and use sympathetic cooling method to suppress the background heating. For an ion array arrange in the z -direction, the transverse trapping frequency ω_x is much greater than the longitudinal trapping frequency ω_z . The trapping frequency ω_z goes to 0 when the number of ion increases, causing the difficulty to scale up the ion trap system. By applying the optical tweezers, we can enhance the mode frequency and hence improve the efficient of cooling.

For large number of ions, the optical tweezers dominate the motional mode frequency. The upper bond of the mode frequency corresponds to the mode frequency when the degree of freedom of the node ions are removed.

Here we conclude our findings and the proposed architecture for large-scale quantum computing. As a linear Paul trap is still regarded as the simplest configuration of implementation compared to other schemes such as ion shuttling and quantum network. Traditionally, a large-scale ion array uses DC voltages to provide longitudinal confinement, which, in order for finite ion separation for individual addressability, must be very weak so that its corresponding motional excitation (phonon) is very hard to be removed. The significance of applying optical tweezers has three folds. First, it raises the frequency of the ground mode from zero, thus stabilizing the ion array and making possible for further laser cooling. Secondly, optical tweezers pin some of the ions so that these pinned ions can serve as “heat blocks.” Therefore, parallel computation is possible by means of the

supposedly collective motion: Gate operations are separated and also protected by optical tweezers. Thirdly, the scheme can be repeatedly extended with only linear increase of the cost. In the following, we summarize in more detail the effects of the optical tweezers on the collective motion including longitudinal and transverse modes as well as the cooling and heating dynamics.



We have shown that the longitudinal and transverse modes behave differently because their characteristic frequencies are separated. Typically, we have $\omega_x \gg \omega_0 \gtrsim \omega_z$, where ω_x and ω_z are transverse and longitudinal trapping frequencies of a Paul trap, respectively, and $\omega_0 = \sqrt{\frac{e^2}{4\pi\epsilon_0} \frac{1}{md_0^3}}$ accounts for residual Coulomb interaction between ions. Therefore, we can expect that the longitudinal mode is more collective and good for heat exchange.

A major source of error comes from the longitudinal motion, where the large displacement lets the ion see spatial variation of the field due to the finite beam size of a Gaussian beam. By applying optical tweezers ($\gtrsim 2\pi \times 500$ kHz for the longitudinal mode), as N gets large (~ 500) while the spacing is kept about d_0 ($\approx 10 \mu\text{m}$), the longitudinal frequency ($\sim 2\pi \times 10$ kHz) is mostly determined by the potential assuming that the “pinned ions” fixed in space instead of the global trap. Thus, the optical tweezers reduce the position fluctuation through stronger confinement than the case without tweezers. Combining the technique of sympathetic cooling, the long ion array can then be stabilized and continuously cooled.

As for the transverse mode, if the applied optical tweezers provide additional confinement for the transverse mode, it becomes a negative factor, which can make the position fluctuation even larger. This is due to the heat blocking effect of the transversely pinned ions. Since the pinned ion has a higher frequency than its neighbors, the heat exchange is less likely to occur. Note that the main source of error associated with the transverse mode is due to the anharmonicity that contributes to the gate fidelity. Unlike the longitudinal part, it has nothing to do with the structural stability of the ion array so the scalability is assured. Such transverse position fluctuation can be suppressed by applying sympathetic cooling within a region sandwiched by two optical tweezers. It is expected that the heat sink in such arrangement can be very efficient so also scalable.

Further, we propose the concept of “local traps” in a large-scale ion chain. We consider only a small segment of the ion array defined by two optical tweezer beams. In other words, the segment is “locally trapped” by two pinned ions. When a quantum gate is operated within the segment, we can just cool this segment instead of cooling the whole ion array. It helps us to reduce the overhead of laser cooling and optical tweezers. For the longitudinal motion, the position fluctuations of the ions in the local trap is nearly halved compared to the case by distributing sympathetically cooled ions without optical tweezers. However, for the transverse mode, the position fluctuation is slightly larger but no more than two times. Note that the actual distribution depends on which ions are chosen to be pinned or sympathetically cooled when the size of the ion chain is finite. Its trend shown here is representative. We also study the relaxation dynamics under the local trap architecture. For both longitudinal and transverse modes, the cooling time is shorter by about an order of magnitude than the case without tweezers.

As future work, we plan to explicitly formulate the local trap idea by employing the open system theory and language, and derive the effective motional spectrum. This can further help us understand and explore the possibility of “local trap sideband cooling.”



Appendix A

Gate design

In this appendix, we describe the pulse shaping scheme [28] to design a two-qubit gate. The procedures have been explicitly discussed in Reference [37]. For completeness of this thesis, we here summarize the method in the following.

Since this scheme is based on the transverse mode, we apply on the two qubit ions bichromatic laser field that generates the spin-dependent forces along the transverse direction. The Hamiltonian of the laser-ion interaction under the Lamb-Dicke limit in the interaction picture is given by

$$\sum_{n,k} \hbar \Omega_n(t) \sin(\mu t) G_n^k \eta^k (a_k^\dagger e^{i\omega_k t} + a_k e^{-i\omega_k t}) \sigma_n^z, \quad (\text{A.1})$$

where $\Omega_n(t)$ is the Rabi frequency of the laser applied on the n th ion, μ is the beatnote frequency of bichromatic field, G_n^k is the mode function coupling the n th ion and the k th mode, $\eta_n^k = |\Delta \mathbf{k}| \sqrt{\frac{\hbar}{2m\omega_k}}$ is the Lamb-Dicke parameter with the wavevector difference of the two beams $|\Delta \mathbf{k}|$, a_k (a_k^\dagger) is the phonon annihilation (creation) operator of the k th mode, σ_n^z is the Pauli-z matrix for the n th ion.

Using the second-order Magnus expansion, we find the evolution operator

$$U(\tau) = \exp \left[i \sum_n \phi_n(\tau) \sigma_n^z + i \sum_{l < n} \phi_{ln}(\tau) \sigma_l^z \sigma_n^z \right], \quad (\text{A.2})$$

where

$$\phi_n = \sum_n \alpha_n^k a^\dagger + \alpha_n^{k*} a \quad (\text{A.3})$$

with

$$\alpha_n^k = \int_0^\tau dt \eta_k G_n^k \Omega_n(t) \sin \mu t e^{i\omega_k t}, \quad (\text{A.4})$$

and

$$\phi_{ln}(\tau) = \int_0^\tau dt_2 \int_0^{t_2} dt_1 \sum_k \eta_l^k \eta_n^k G_l^k G_n^k \Omega_l(t_2) \Omega_n(t_1) \sin \mu t_2 \sin \mu t_1 \sin \omega_k(t_2 - t_1). \quad (\text{A.5})$$

Suppose the gate implemented involves the i th and j th ions. We set $\Omega_i(t) = \Omega_j(t) = \Omega(t)$, and $\Omega_n(t) = 0$ for others.

To construct a CPF gate, we need to find appropriate $\Omega(t)$ that satisfies the constraints

$$\phi_{i(j)} = 0, \quad (\text{A.6a})$$

$$\phi_{ij}(\tau) = \frac{\pi}{4}. \quad (\text{A.6b})$$

A straightforward strategy is to chop $\Omega(t)$ into M equal segments. We have $\Omega(t) = \Omega_m$ when $\tau_{m-1} < t < \tau_m$ with $\tau_m = m\tau/M$. Equations (A.6) give $2N + 1$ constraints. To exactly fulfill A.6, we need $2N + 1$ independent parameters so that $M = 2N + 1$.

Instead of exactly eliminating $\phi_{i(j)}$, we can use $M \leq 2N + 1$ segments and maximize the fidelity. The fidelity is defined by

$$F = \langle \psi_f | \text{Tr}_m \{ U(\tau) (|\psi_0\rangle\langle\psi_0| \otimes \rho_{\text{th}}) U^\dagger(\tau) \} | \psi_f \rangle, \quad (\text{A.7})$$

where the final qubit state $|\psi_f\rangle = e^{i\pi\sigma_i^z\sigma_j^z/4} |\psi_0\rangle$ with the initial qubit state $|\psi_0\rangle$, ρ_{th} is the density matrix of the phonon, and Tr_m denotes the trace over all phonon Fock states.

Choose a typical initial qubit state $|\psi_0\rangle = (|0\rangle_i + |1\rangle_i) \otimes (|0\rangle_j + |1\rangle_j)$, and assume that the phonons are in the thermal state $\rho_{\text{th}} = \bigotimes_{k=0}^N \frac{1}{1-e^{-\beta\hbar\omega_k}} \sum_{n_k=0}^{\infty} e^{-n_k\hbar\omega_k} |n_k\rangle\langle n_k|$. Then



the infidelity becomes

$$\delta F = 1 - F = \frac{1}{8}(6 - 2(\Gamma_i + \Gamma_j) - \Gamma_+ - \Gamma_-), \quad (\text{A.8})$$



where

$$\Gamma_{i(j)} = \exp\left(-\sum_k |\alpha_{i(j)}^k|^2 \bar{\beta}_k/2\right), \quad (\text{A.9a})$$

$$\Gamma_{\pm} = \exp\left(-\sum_k |\alpha_i^k \pm \alpha_j^k|^2 \bar{\beta}_k/2\right), \quad (\text{A.9b})$$

with $\bar{\beta}_k = \coth\left(\frac{\hbar\omega_k}{k_B T}\right)$. Our goal now is to find a vector $X = (\Omega_1, \Omega_2, \dots, \Omega_M)^\top$ to minimize Equation (A.8) under the constraints Equation (A.6b).

We can use the quadratic minimization method to simplify the calculation. We focus on the infidelity $\delta F \sim 0$, which corresponds to $\alpha_{i(j)}^k \sim 0$. We take Taylor expansion $e^{-x} \approx 1 - x + O(x^2)$ for Γ 's. Then the infidelity becomes

$$\delta F \approx \frac{1}{4} \sum_k \bar{\beta}_k (|\alpha_i^k|^2 + |\alpha_j^k|^2). \quad (\text{A.10})$$

Define $H_i^k = (H_{i1}^k, H_{i2}^k, \dots, H_{iM}^k)^\top$ with $H_{im}^k = \eta^k G_i^k \int_{\tau_{m-1}}^{\tau_m} dt e^{i\omega_k t} \sin \mu t$. Then $\alpha_i^k = H_i^k \cdot X$, where \cdot denotes the inner product. Further, $\sum_k \bar{\beta}_k |\alpha_i^k|^2$ can be rewritten as $X^\top A^i X$ with the matrix element $A_{mm'}^i = \sum_k \bar{\beta}_k H_{im}^k H_{im'}^{k*}$. Define $A = \frac{1}{4}(A^i + A^j)$. Finally we get

$$\delta F = X^\top A X. \quad (\text{A.11})$$

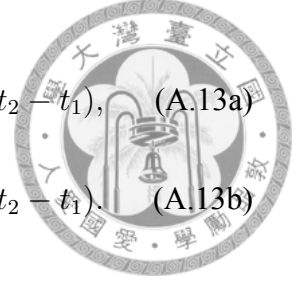
The conditional phase ϕ_{ij} (Equation (A.5)) can be also expressed in the matrix form

$$\phi_{ij} = X^\top B X, \quad (\text{A.12})$$

where the matrix $B_{mm'} = P_{mm'}/2 + Q_m \delta_{mm'}$ with the definition

$$P_{mm'} = \int_{\tau_{m-1}}^{\tau_m} dt_2 \int_{\tau_{m'-1}}^{\tau_{m'}} dt_1 \sum_k \eta_l^k \eta_n^k G_l^k G_n^k \sin \mu t_2 \sin \mu t_1 \sin \omega_k(t_2 - t_1), \quad (\text{A.13a})$$

$$Q_m = \int_{\tau_{m-1}}^{\tau_m} dt_2 \int_{\tau_{m-1}}^{t_2} dt_1 \sum_k \eta_l^k \eta_n^k G_l^k G_n^k \sin \mu t_2 \sin \mu t_1 \sin \omega_k(t_2 - t_1). \quad (\text{A.13b})$$



To minimize Equation (A.11) with constraint Equation (A.12), we use Lagrange undetermined multiplier method. The modified infidelity $\delta F^* = X^\top AX + \lambda X^\top BX$. To find minimum value of δF^* , we make $\frac{\partial \delta F^*}{\partial X^\top} = 0$, which gives a generalized eigenvalue equation $AX = \lambda BX$. By solving the eigenvectors and checking the associated infidelity, we can obtain the proper X , which will be further re-scaled such that $\phi_{ij} = \pi/4$.



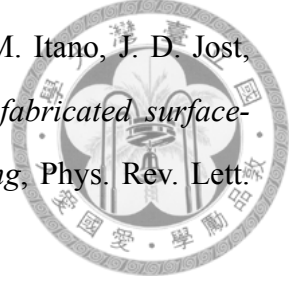
Bibliography

- [1] P. Shor, *Algorithms for quantum computation: discrete logarithms and factoring*, in *Proceedings 35th Annual Symposium on Foundations of Computer Science* (IEEE Comput. Soc. Press, 1994) pp. 124–134.
- [2] J. Proos and C. Zalka, *Shor's discrete logarithm quantum algorithm for elliptic curves*, *Quantum Info. Comput.* **3**, 317–344 (2003), arXiv:quant-ph/0301141 .
- [3] T. Kleinjung, J. W. Bos, A. K. Lenstra, D. A. Osvik, K. Aoki, S. Contini, J. Franke, E. Thomé, P. Jermini, M. Thiéard, P. Leyland, P. L. Montgomery, A. Timofeev, and H. Stockinger, *A heterogeneous computing environment to solve the 768-bit RSA challenge*, *Cluster Computing* **15**, 53–68 (2012).
- [4] E. Gerjuoy, *Shor's factoring algorithm and modern cryptography. An illustration of the capabilities inherent in quantum computers*, *American Journal of Physics* **73**, 521–540 (2005), arXiv:quant-ph/0411184 .
- [5] D. P. DiVincenzo, *The Physical Implementation of Quantum Computation*, *Fortschritte der Physik* **48**, 771–783 (2000), arXiv:quant-ph/0002077 .
- [6] W. Paul, *Electromagnetic traps for charged and neutral particles*, *Rev. Mod. Phys.* **62**, 531–540 (1990).
- [7] S. Olmschenk, K. C. Younge, D. L. Moehring, D. N. Matsukevich, P. Maunz, and C. Monroe, *Manipulation and detection of a trapped Yb^+ hyperfine qubit*, *Phys. Rev. A* **76**, 1–9 (2007), arXiv:0708.0657 .

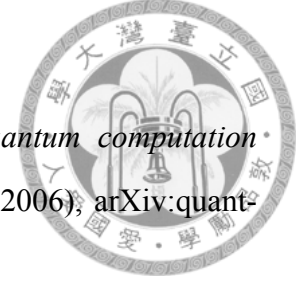
- [8] J. I. Cirac and P. Zoller, *Quantum computations with cold trapped ions*, Phys. Rev. Lett. **74**, 4091–4094 (1995), arXiv:quant-ph/0305129 .
- [9] A. Sørensen and K. Mølmer, *Quantum Computation with Ions in Thermal Motion*, Phys. Rev. Lett. **82**, 1971–1974 (1999), arXiv:quant-ph/9810039 .
- [10] A. Sørensen and K. Mølmer, *Entanglement and quantum computation with ions in thermal motion*, Phys. Rev. A **62**, 1–11 (2000), arXiv:quant-ph/0002024 .
- [11] S. Debnath, N. M. Linke, C. Figgatt, K. A. Landsman, K. Wright, and C. Monroe, *Demonstration of a small programmable quantum computer with atomic qubits*, Nature **536**, 63–66 (2016), arXiv:1603.04512 .
- [12] T. Monz, D. Nigg, E. A. Martinez, M. F. Brandl, P. Schindler, R. Rines, S. X. Wang, I. L. Chuang, and R. Blatt, *Realization of a scalable Shor algorithm*, Science **351**, 1068–1070 (2016), arXiv:1507.08852 .
- [13] D. Kielpinski, C. Monroe, and D. J. Wineland, *Architecture for a scalable ion-trap quantum computer*, Nature **417**, 709–711 (2002).
- [14] L.-M. Duan and C. Monroe, *Colloquium: Quantum networks with trapped ions*, Rev. Mod. Phys. **82**, 1209–1224 (2010), arXiv:1506.00985 .
- [15] C. Schneider, M. Enderlein, T. Huber, and T. Schaetz, *Optical trapping of an ion*, Nature Photonics **4**, 772–775 (2010), arXiv:1001.2953 .
- [16] D. Kielpinski, B. King, C. Myatt, C. Sackett, Q. Turchette, W. Itano, C. Monroe, D. J. Wineland, and W. Zurek, *Sympathetic cooling of trapped ions for quantum logic*, Phys. Rev. A **61**, 032310 (2000).
- [17] G.-D. Lin and L.-M. Duan, *Sympathetic cooling in a large ion crystal*, Quantum Information Processing **15**, 5299–5313 (2016), arXiv:1511.02463 .
- [18] M. G. Raizen, J. M. Gilligan, J. C. Bergquist, W. M. Itano, and D. J. Wineland, *Ionic crystals in a linear Paul trap*, Phys. Rev. A **45**, 6493–6501 (1992).



- [19] S. Seidelin, J. Chiaverini, R. Reichle, J. J. Bollinger, D. Leibfried, J. Britton, J. H. Wesenberg, R. B. Blakestad, R. J. Epstein, D. B. Hume, W. M. Itano, J. D. Jost, C. Langer, R. Ozeri, N. Shiga, and D. J. Wineland, *Microfabricated surface-electrode ion trap for scalable quantum information processing*, Phys. Rev. Lett. **96**, 1–4 (2006), arXiv:quant-ph/0601173 .
- [20] A. Barenco, C. H. Bennett, R. Cleve, D. P. Divincenzo, N. Margolus, P. Shor, T. Sleator, J. A. Smolin, and H. Weinfurter, *Elementary gates for quantum computation*, Phys. Rev. A **52**, 3457–3467 (1995), arXiv:quant-ph/9503016 .
- [21] H. Häffner, C. F. Roos, and R. Blatt, *Quantum computing with trapped ions*, Physics Reports **469**, 155–203 (2008), arXiv:0809.4368 .
- [22] F. Schmidt-Kaler, H. Häffner, M. Riebe, S. Guide, G. P. T. Lancaster, T. Deuschle, C. Becher, C. Roos, J. Eschner, and R. Blatt, *Realisation of the Cirac-Zoller controlled-NOT quantum gate*, Nature **422**, 408–411 (2003).
- [23] C. A. Sackett, D. Kielpinski, B. E. King, C. Langer, V. Meyer, C. J. Myatt, M. Rowe, Q. A. Turchette, W. M. Itano, D. J. Wineland, and C. Monroe, *Experimental entanglement of four particles*, Nature **404**, 256–259 (2000), arXiv:quant-ph/0312197 .
- [24] T. Monz, P. Schindler, J. T. Barreiro, M. Chwalla, D. Nigg, W. A. Coish, M. Harlander, W. Hänsel, M. Hennrich, and R. Blatt, *14-qubit entanglement: Creation and coherence*, Phys. Rev. Lett. **106**, 1–4 (2011), arXiv:1009.6126 .
- [25] G. J. Milburn, S. Schneider, and D. F. V. James, *Ion Trap Quantum Computing with Warm Ions*, Fortschritte der Physik **48**, 801–810 (2000).
- [26] P. J. Lee, K.-A. Brickman, L. Deslauriers, P. C. Haljan, L.-M. Duan, and C. Monroe, *Phase Control of Trapped Ion Quantum Gates*, J. Opt. B. **371**, 21 (2005), arXiv:quant-ph/0505203 .
- [27] D. Leibfried, B. DeMarco, V. Meyer, D. Lucas, M. Barrett, J. Britton, W. M. Itano, B. Jelenković, C. Langer, T. Rosenband, and D. J. Wineland, *Experimental demon-*



stration of a robust, high-fidelity geometric two ion-qubit phase gate, *Nature* **422**, 412–415 (2003).



- [28] S.-L. Zhu, C. Monroe, and L.-M. Duan, *Trapped ion quantum computation with transverse phonon modes*, *Phys. Rev. Lett.* **97**, 050505 (2006), arXiv:quant-ph/0601159 .
- [29] C. Monroe, D. M. Meekhof, B. E. King, S. R. Jefferts, W. M. Itano, D. J. Wineland, and P. Gould, *Resolved-sideband Raman cooling of a bound atom to the 3D zero-point energy*, *Physical Review Letters* **75**, 4011–4014 (1995).
- [30] G.-D. Lin, S.-L. Zhu, R. Islam, K. Kim, M.-S. Chang, S. Korenblit, C. Monroe, and L.-M. Duan, *Large-scale quantum computation in an anharmonic linear ion trap*, *Europhys. Lett.* **86**, 60004 (2009), arXiv:0901.0579 .
- [31] A. M. Steane, *The ion trap quantum information processor*, *Appl. Phys. B* **64**, 623–642 (1997), arXiv:quant-ph/9608011 .
- [32] D. H. E. Dubin, *Theory of structural phase transitions in a trapped Coulomb crystal*, *Phys. Rev. Lett.* **71**, 2753–2756 (1993).
- [33] H. Totsuji and J.-L. Barrat, *Structure of a nonneutral classical plasma in a magnetic field*, *Phys. Rev. Lett.* **60**, 2484–2487 (1988).
- [34] Q. A. Turchette, D. Kielpinski, B. E. King, D. Leibfried, D. M. Meekhof, C. J. Myatt, M. A. Rowe, C. A. Sackett, C. S. Wood, W. M. Itano, C. Monroe, and D. J. Wineland, *Heating of trapped ions from the quantum ground state*, *Phys. Rev. A* **61**, 063418 (2000), arXiv:quant-ph/0002040 .
- [35] C. Gardiner and P. Zoller, *Quantum Noise: A Handbook of Markovian and Non-Markovian Quantum Stochastic Methods with Applications to Quantum Optics* (Springer, 2004).
- [36] S.-L. Zhu, C. Monroe, and L.-M. Duan, *Arbitrary-speed quantum gates within large*

ion crystals through minimum control of laser beams, Europhys. Lett. **73**, 485–491 (2006), arXiv:quant-ph/0508037 .

- [37] G.-D. Lin, *Quantum Simulation with Ultracold Atoms and Trapped Ions*, Ph.D. thesis, University of Michigan (2010).

